20 May 2016
Updated 2023

ENHANCING POWER GENERATION EFFICIENCY WITH A STIRLING GENERATOR AND TROUGH SOLAR: A CASE STUDY

Introduction

Stirling generators, a type of Stirling engine, have gained popularity for their ability to efficiently convert heat into mechanical work. This case study explores the implementation of a 200kW Stirling generator plant in Thailand. This study details the project's goals, implementation, and the results achieved.

Project Overview

The decision to design the Stirling Generator was fundamentally driven by the recognition that contemporary solar energy capture technologies harness only a fraction of the solar energy potential available. Existing solutions predominantly focus on capturing the visible spectrum of sunlight, while largely neglecting the valuable ultraviolet (UV) and infrared (IR) spectrums.

Substantial advancements in the field of light and optics, resulting from extensive research in various projects, provided the capability to engineer a system that not only harnessed the visible spectrum but also effectively captured the UV and IR spectra. This distinctive and proprietary feature distinguishes the Stirling Generator system, as its solar collectors have the remarkable ability to harness up to 92% of the solar energy that reaches the Earth's surface. In stark contrast, Concentrated Solar Power (CSP) systems can capture a maximum of 60%, while conventional photovoltaic (PV) solar farms, as currently employed, only achieve a modest 16-22% capture efficiency.

A high-level outline of the project is detailed below.

I. **Inception of the Project**
The project's primary objective at its outset was to devise a method aimed at harnessing the full spectrum of solar energy to generate power. Rigorous research and extensive experimentation, however, unequivocally revealed that the attainment of 100% solar energy utilization was an unattainable goal at that juncture. In March 2015, photovoltaic modules could merely capture approximately 16% of the sun's energy, and even the most advanced Concentrated Solar Plants (CSP) could extract only 60% of solar energy. Consequently, the project team concurred that achieving up to 92% solar energy capture under controlled laboratory conditions would be deemed an acceptable benchmark, thereby allowing the project to proceed.

II. **Energy Storage Endeavors**
The subsequent phase involved the storage of the harvested solar energy, with a focus on thermal storage. Initially, molten salt appeared to be the natural choice for this purpose. However, contemporary technologies available at that time fell short of meeting the desired performance criteria. To address this limitation, an entirely new formulation for the molten salt compound was conceived, verified, and refined through a series of iterative field experiments. Subsequently, it was determined that molten salt-based thermal storage systems were most suited for cold climates, while hot climates presented a preference for oil-based systems

utilizing steam generation. This innovation extended its applicability to organizations or locations already engaged in steam production, thereby offering potential beneficiaries.

III. Addressing Market Requirements

The final stage of the project aimed to effectively cater to market demands. In many markets, there was a conspicuous lack of enthusiasm for thermal energy solutions. Therefore, the logical strategy, particularly in the Asian context, was to maximize electricity generation from stored thermal energy, rendering it readily available as needed. Two core principles were evaluated for this purpose: the Organic Rankine Cycle (ORC) and the venerable Stirling Generator principle.

The ORC, commercially available from various global manufacturers, was considered; however, its operational efficiency at lower temperatures relegated it to a secondary position when weighed against the Stirling Generator principle. While the Stirling Generator principle exhibited the potential for significantly higher efficiency, it necessitated an upgrade to meet the project's demands. Remarkably, within a matter of weeks, the principle was not only retained but also elevated to a level of refinement that could rival the research endeavors of most esteemed academic institutions, particularly considering the limited timeframe within which it was accomplished. This remarkable achievement was acknowledged by experts as "The most astonishing interpretation of a Stirling Generator ever witnessed." Consequently, a prototype was constructed and prepared for commissioning.

IV. Project Implementation and Success

In 2015, the project reached a significant milestone with the successful establishment of a 200kW continuous electricity supply Stirling Generator plant. This facility, located in Bangkok, Thailand, has remained in continuous operation since its deployment, consistently delivering the projected yield of an average of 200 kW per hour, totaling an average of 4,800 kWh per day (over a 24-hour period) without any observable degradation in performance.

Goals

1. **Increase Efficiency**: The primary goal was to improve the overall efficiency of power generation, thus reducing operational costs and environmental impact.
2. **Reduce Emissions**: By relying on a Stirling generator, the aim was to decrease greenhouse gas emissions associated with power generation.
3. **Reliability**: To create a reliable power generation system to ensure uninterrupted electricity supply.

Global Development

Over the past three decades, companies have effectively employed Stirling generators with notable success. These generators, based on the Stirling engine's principles, have been utilized in various applications, including power generation, as they offer several advantages such as high efficiency, low emissions, and quiet operation.

Stirling engines, the driving force behind these generators, operate by cyclically compressing and expanding a fixed amount of gas, typically hydrogen or helium. As the gas is heated and cooled, it undergoes expansion and compression, which in turn drives the pistons to generate mechanical energy.

While Stirling engines have been in use for quite some time, recent advancements in this technology have significantly improved the efficiency and performance of these systems. Engineers and researchers have focused on enhancing the design and materials used, enabling these generators to achieve greater power output with higher reliability and reduced maintenance requirements.

One of the critical recent advancements involves improvements in the materials used for constructing Stirling engines. Advances in material science have led to the development of more durable and heat-resistant materials, allowing engines to operate at higher temperatures without compromising their performance or longevity. This has contributed to increased efficiency and power output while maintaining durability and reliability over extended periods.

Moreover, ongoing research has led to the optimization of the engine's design, resulting in better thermal efficiency and overall performance. Enhanced heat exchangers, improved insulation, and more precise control systems have further contributed to increased efficiency, allowing these generators to produce more electricity for a given amount of heat input.

These advancements have made Stirling generators even more appealing across a variety of applications, particularly in sustainable energy systems like solar power plants, biomass energy, and combined heat and power systems. Their ability to operate quietly, with lower emissions, and higher efficiency positions them as a promising technology for both current and future energy needs.

Name	Year	Net Electricity	System Efficie	Location	Diameter	Type	Surface	Reflectance	Tracking	Engine Compar	Engine Type	Engine (V	Working Fluid	Pressure	Gas Temp
Advanco' Vanguard System	1984-1988	25 kW	29.4% @ 760° C Gas Temp	California	10.57m	Faceted Glass Mirrors	Glass/Silver	90.50%	Excentric	Company 1	Kinematic		Hydrogen	20 MPa	720° C
Schlaich-Bergermann Partner (50 kW System)	1984-1988	52.5 kW	23.10%	Riyadh, Saudi Arabia	17m	Stretched Membrane	Glass/Silver on Stainless Steel	92%	Az-el	Company 2	Kinematic		Hydrogen	15 Mpa	620° C
McDonnell-Douglas	1984-1988	25 kW	29-30%	California, Georgia, Nevada	10.57m	Faceted Glass Mirrors	Glass/Silver	91%	Az-el	Company 3	Kinematic	25 kW	Hydrogen	20 MPa	720° C
Schlaich-Bergermann Partner (9 kW System)	1991	9 kW	20.30%	3 built in Spain, 2 built in Germany	7.5m	Stretched Membrane	Glass/Silver on Stainless Steel	94%	Polar	Company 4	Free Piston	9kW	Helium	15 Mpa	630° C
Cummins Power Generation (7.5 kW System)	1992	7.5 kW	19%	California, Texas, Pennsylvania	7.0m	Stretched Membrane	Aluminum Plastic Film	78-85%	Polar	Company 5	Kinematic	9 kW	Helium	4 Mpa	629° C
Aisin Seiki Miyako Island System	1992	8.5 kW	16%	Mijako, Japan						Company 6	Kinematic	30 kW	Hellum	14.5 Mpa	683° C
Science Applications International Corporation	1993	25 kW	Depends on concentrator used	Sandia National Laboratories, TBC						Company 7	Kinematic	25 kW	Hellum	12 Mpa	720° C
Stirling Engine Systems (SES)	1996	25 kW	30%	Phoenix, USA	11.28m	Commercial Grade Float	Silvered on Backside	>90%	Az-el	Company 8	Free Piston	27 kW	Hydrogen/Helium	20 MPa	720° C
EuroDish	1998	10 kW	22-24.5%		8.5m	Stretched Membrane	Glass Fibre Resin	94%	Az-el	Company 9	Single Acing	8.4 kW	Helium	20-150 bar	650°C
Infinia Corporation	2007	32 kW	24%	US, Europe, India, Yuma	4.7m	Silver Coated Glass Mirrors	Glass Fibre Reinforced Plastic	85%	Az-el	Company 10	Free Piston	3 kW	Hellum		
SG4 500-m2 Solar Dish (ANU)	2008	50 kW		Whyalla, South Australia	25m	Mirror Panels	GlassGlass-on-Metal Laminate Mirrors	90.50%	Az-el	Company 11			Air	5 Mpa	550° C
HelioFocus	2011		24%	Israel		Solar Mirrors (2 axes)	Simple Carbon Steel	95%	Az-el	Company 12	Steam Turbines	130kW	Air		1000°C
Solar Cell SouthWest Solar	2011	5kW		Phoenix, Arizona, USA	20m	Mirror Panels	Flat Metal Structure			Company 13		80 kW	Oil & Liquid Free		
Solar Systems CS500 Dense Array CPV Dish System	2013	35 kW	40%	Mildura	15m	Mirror Panels			Az-el	Company 14					

Table 1.1 Design and Performance Specification for Dish/Stirling Systems (Ref. 1.)

Solar Thermal Energy: A Fully Developed and Efficient Solution

Solar thermal power plants are emerging as a crucial component in the future of energy supplies. Although research and development initiatives were initiated in the United States during the 1980s, a significant hiatus interrupted progress in this field until recent years. Nevertheless, solar thermal power plants exhibit remarkable efficiency and represent a climate-friendly and resource-efficient approach to energy production. In regions blessed with abundant sunlight, they offer a viable and profitable investment option.

In a conventional power plant, the generation of steam relies on the combustion of substances like coal or oil. The resultant high-pressure steam propels a turbine that, in turn, drives an electricity generator. Following this, the steam is condensed back into water and returned to the steam generator.

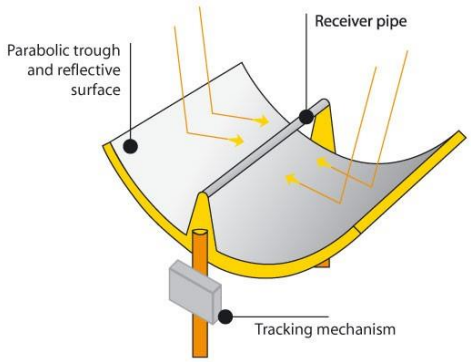

Figure 1.1: Parabolic Trough Collector

Solar thermal power plants adhere to the same foundational principles as conventional power plants, albeit with a key distinction. They harness solar energy, provided cost-free by the sun, to fulfill the energy demands of the steam generator. Simplistically, the process involves the concentration of sunlight by parabolic mirrors onto an absorber pipe located along a focal line. Sunlight is thereby converted into heat and transferred to a heat transfer medium, which may include thermal oil, liquefied salt, or water. This method facilitates the attainment of high temperatures, often reaching up to 760°C (Ref. 2). Analogous to a conventional power plant, the resulting steam powers a turbine connected to a generator.

Variability in solar radiation is accommodated through the integration of a heat storage system and a combination with alternative energy sources, such as biomass or fossil fuels. These measures guarantee a year-round supply of energy, mitigating the impact of fluctuations in solar irradiance.

Solar thermal power plants, particularly those utilizing parabolic trough collectors, rely on mature and proven technology. They have been subjected to practical implementation and have consistently demonstrated their capacity to provide a reliable and unwavering energy supply.

Solar-Generated Process Heat: An Ecological, Economical, and Forward-Looking Solution

Solar-generated process heat stands out as an exceptionally sustainable method of energy recovery, offering substantial benefits in terms of environmental impact, resource conservation, and availability. Parabolic trough technology, renowned for its efficiency, transforms direct solar radiation into valuable thermal energy. Notably, the utilization of direct steam generation through parabolic trough systems permits the attainment of elevated operating temperatures, reaching up to 400°C, a range well-suited for diverse industrial processes.

Solar-generated process heat represents a promising avenue for sustainable energy recovery, characterized by its advantageous ecological, economic, and forward-looking attributes. One of the distinguishing features of solar-generated process heat is its reliance on parabolic trough technology. This technology excels at harnessing direct solar radiation and converting it into valuable thermal energy. The capacity to operate at higher temperatures is a crucial factor for meeting the demands of industrial processes.

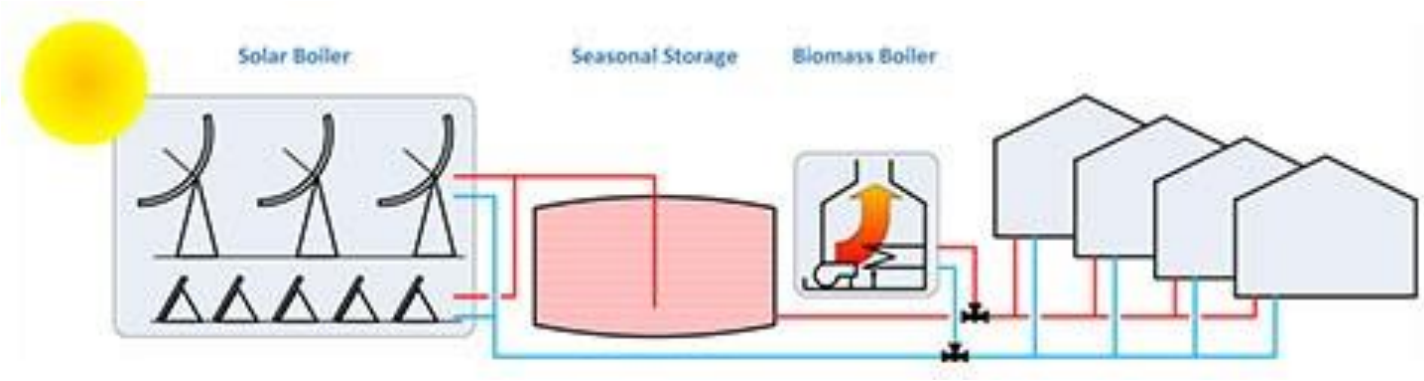

Figure 1.2: Solar-Generated Process Heat Principle

In industrial settings, the demand for process heat constitutes a significant portion of the overall energy consumption. Solar-generated process heat is introduced as a viable and environmentally friendly means to address this demand.

Already in use in local heating plants in Denmark, this technology is explored as a means to provide thermal energy in storage systems. Parabolic troughs are recognized for their suitability in warmer regions, where they can be integrated into district cooling systems. This approach is presented as both economical and highly recommended, particularly for larger-scale implementations.

The utilization of solar-generated process heat stands as a promising solution, addressing the substantial energy demands of industrial processes in an ecologically sound and economically beneficial manner.

Standardization of Solar Heat Integration for Industrial Processes

The objective is to develop a standardized, modular interface that enhances the cost-effectiveness of solar process heat systems. Traditionally, the customized planning and on-site production of components have contributed significantly to costs and potential errors. To address this, test units were developed and evaluated, representing various output sizes, temperature levels, and heat transfer media. A standardized, modular balance of plant (BoP)was designed as the interface between the solar field and industrial process heating systems. The BoP accommodates multiple heat transfer media in the primary and secondary circuits, ensuring flexibility and efficiency. The new power transfer concept allows for the integration of alternative heat transfer media and heat storage units to enhance system stability.

The project unfolds in several work packages, encompassing concept development, detailed planning, BoP design and manufacturing, test and instrumentation planning, installation and testing of units, cost reduction analysis, and preparation for commercial adoption through feasibility studies.

I. **Objectives:** The primary goals include developing and evaluating test units that represent various practical scenarios, considering output sizes, temperature levels, and heat transfer media. These test units serve as the foundation for a modular and scalable balance of plant (BoP) that acts as an interface between the solar field and industrial process heating systems. The BoP is designed to offer flexibility and efficiency by accommodating various heat transfer media in both primary and secondary circuits.

II. **Enhancing Flexibility:** The innovative power transfer concept allows for the integration of alternative heat transfer media, such as steam or hot water. Additionally, plans are in place to connect heat storage units, ensuring operational stability even during periods of reduced solar radiation.

III. **Testing and Validation:** Testing and validation of power transfer stations in commercial projects is focused on connecting collector fields. These activities are conducted utilizing the project development and planning conditions to create a standardized BoP concept.

IV. **Work Package Structure:** The project is structured into distinct work packages, each with a specific focus. These packages cover concept development (Work Package 2), detailed planning (Work Package 3), BoP design and manufacturing (Work Package 4), test and instrumentation planning (Work Package 5), installation and testing of units (Work Package 6), cost reduction analysis (Work Package 7), and preparation for commercial adoption through feasibility studies (Work Package 8).

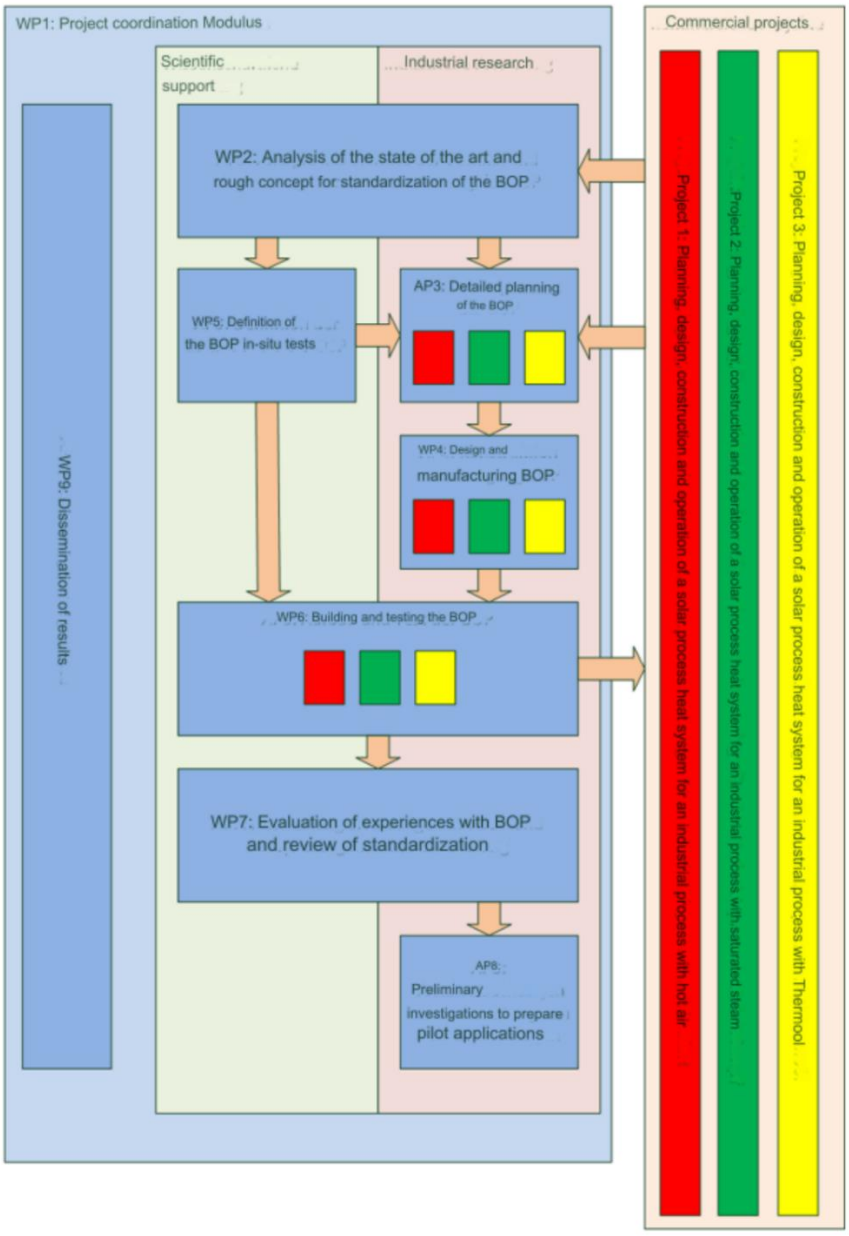

Figure 1.3: Work Packages of the Project (Ref. 3)

The pursuit of standardization in solar heat integration for industrial processes signifies a transformative approach in enhancing the efficiency and cost-effectiveness of solar process heat systems. The modular and scalable BoP, coupled with testing in commercial projects, holds the potential to revolutionize the industry and pave the way for a more sustainable and economically feasible future.

Image 1.1 Balance of Plant (BoP) with Collector (Ref. 3)

Plant Location

Thailand was selected as the test site for the Stirling generator plant due to its abundant solar resource, favorable climate conditions, environmental benefits, economic viability, and the potential to serve as a model for similar projects in the region and beyond.

I. **Abundant Solar Resource:** Bangkok enjoys a tropical climate with plentiful sunshine throughout the year. The region experiences a high level of solar irradiance, which is essential for the efficient operation of solar-based technologies like Stirling generators.
II. **Steady Temperature Conditions:** The consistent warm and sunny climate in Bangkok ensures a stable temperature range, which is favorable for the operation of Stirling engines. These engines perform optimally when exposed to relatively constant temperature conditions.
III. **Year-Round Operation:** The reliable availability of sunlight in Bangkok enables year-round operation of the Stirling generator plant. This consistency in energy production is crucial for commercial viability and energy supply.
IV. **Reduced Heating Needs:** Stirling engines benefit from temperature differentials, which can be more pronounced in regions with warm climates like Bangkok. This leads to enhanced thermal efficiency and increased electricity generation.
V. **Environmental Impact:** Using a test site in Bangkok allows for environmentally conscious testing and operation. Solar energy is a clean and sustainable power source, aligning with global efforts to reduce greenhouse gas emissions and combat climate change.
VI. **Economic Viability:** Solar energy projects in sun-rich regions, such as Bangkok, often prove economically viable due to the high solar resource, which can lead to a favorable return on investment for such projects.

VII. **Demonstration of Technology:** Bangkok's test site can serve as a showcase for the technology's capabilities. The consistent performance in a diverse climate can demonstrate the adaptability and reliability of Stirling generators to potential investors and other regions.

VIII. **Local Expertise:** The presence of local expertise and support in the renewable energy sector can be advantageous. Collaborating with local professionals and organizations can facilitate the project's success and integration with the local energy infrastructure.

IX. **Grid Integration:** Bangkok's well-developed electrical grid infrastructure makes it easier to integrate the Stirling generator plant into the existing power distribution network.

X. **Market Opportunities:** Thailand's growing interest in renewable energy and sustainable solutions creates a favorable market environment for the adoption and deployment of innovative technologies like Stirling generators.

Technical developments

The team developed a parabolic trough collector made with a combination of glass fiber composite material and an efficient thin-film glass mirror. With this, we have achieved higher operating temperatures, a simpler construction, a significant reduction in weight and panel costs and thereby, ultimately an increase in the efficiency of the whole power plant.

I. **Parabolic troughs made from composite materials**
Simplicity of construction, together with the use of new materials and material combinations, allows mass production of an optical instrument with higher precision, whilst simultaneously greatly reducing weight and costs.

II. **Direct steam generation**
This is the first time this technology is being employed. The team has refined the operating concept and tested it in plants in Denmark and Thailand. The direct evaporation of water means the use of expensive and environmentally unfriendly combination of thermal oil plus heat exchanger can be avoided. This considerably increases efficiency compared to current technology, as well as lowering costs.

III. **Combined heat and power**
The power plant technology offers the option of combining heat and power generation, which increases performance and expands the current operating concepts in the market that supply either electricity or process heating.

Stirling Generator

The core element of the envisaged distributed combined heat and power system in this project is the Stirling Generator. The conceptualized system is tailored for generating power at a residential scale and integrates energy storage to ensure consistent power output even when confronted with variable solar resources. Additionally, the waste heat emanating from the engine finds purpose in local heating applications, further enhancing the overall system efficiency.

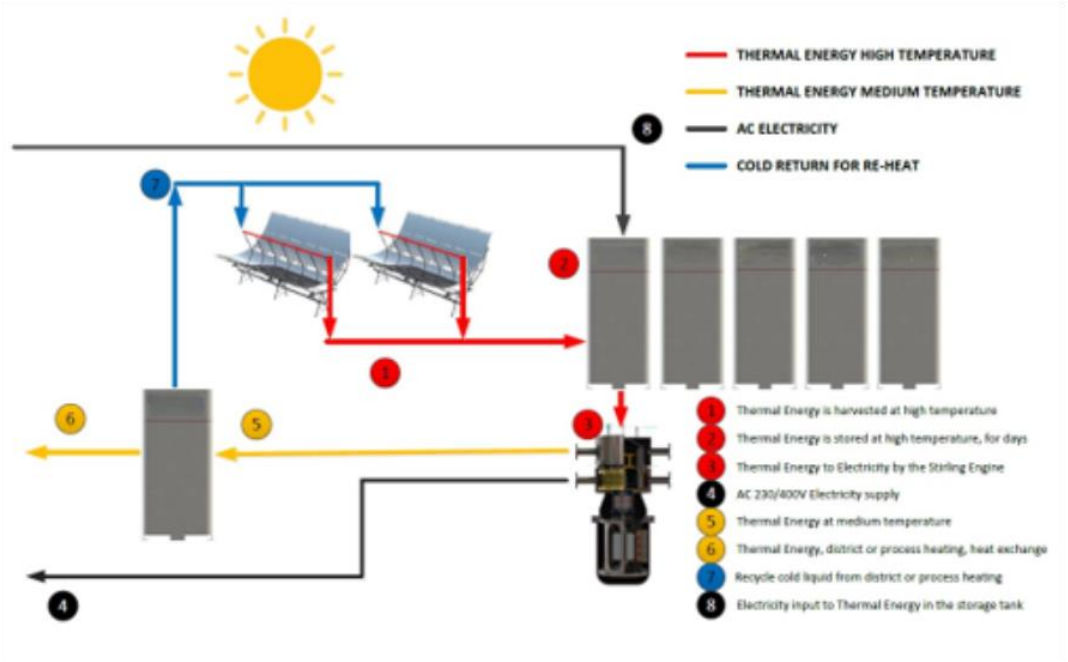

Figure 1.4 Simplified Principle

A visual representation of the solar thermal system is depicted in Figure 1.4. The essential components of the system encompass a passive solar collector, a hot thermal storage subsystem, the Stirling generator, and an optional waste heat capture module. The system is designed with evacuated tube solar collectors in mind due to their capacity to provide high-temperature input heat and efficiency, while remaining cost-effective. These collectors do not require tracking mechanisms to minimize component count and cost. Nonetheless, passive concentrators were introduced and tested to enhance efficiency. Alternatively, in situations where solar energy is insufficient or requires balancing, on-site combustion can serve as a thermal energy source. The thermal energy storage component can be achieved with readily available and cost-effective hot water tanks commonly used in residential settings. Supporting components encompass piping, fluid pumps, and heat exchangers to facilitate heat transfer between system elements and streams.

The majority of the system is intended to be assembled using commercially available components, with the aim of reducing costs and ensuring simplicity. The notable exception is the Stirling engine, which necessitates substantial engineering efforts to attain high performance. The Stirling engine stands as the linchpin of the entire system.

The Stirling engine operates as a heat engine, employing the Stirling Cycle to transform thermal energy flow into mechanical energy. Conversely, it can also function in reverse as a heat pump, leading to the opposite energy conversion process. A distinctive feature of the Stirling Cycle is its closed-loop nature, where the internal working fluid is contained and isolated from the external energy source. Consequently, heat exchangers are employed to facilitate the transfer of thermal energy: from an external hot-side source into the engine and from the engine to an external cold-side sink.

The Stirling Cycle adheres to thermodynamic principles and is inherently governed by the Carnot Efficiency, as expressed in Equation 1.1 (Ref. 8):

$$\eta = 1 - \frac{T_C}{T_H}$$

Equation 1.1

Here, η represents the maximum theoretical efficiency, TC signifies the temperature of the cold-side reservoir, and TH denotes the temperature of the hot-side reservoir.

Characterizing the Stirling Cycle as a gas cycle, its behavior can be effectively represented by a P-V diagram, depicting the relationship between internal pressure and internal volume throughout a single cycle of the engine. An illustrative P-V diagram is provided in Figure 1.5 for reference.

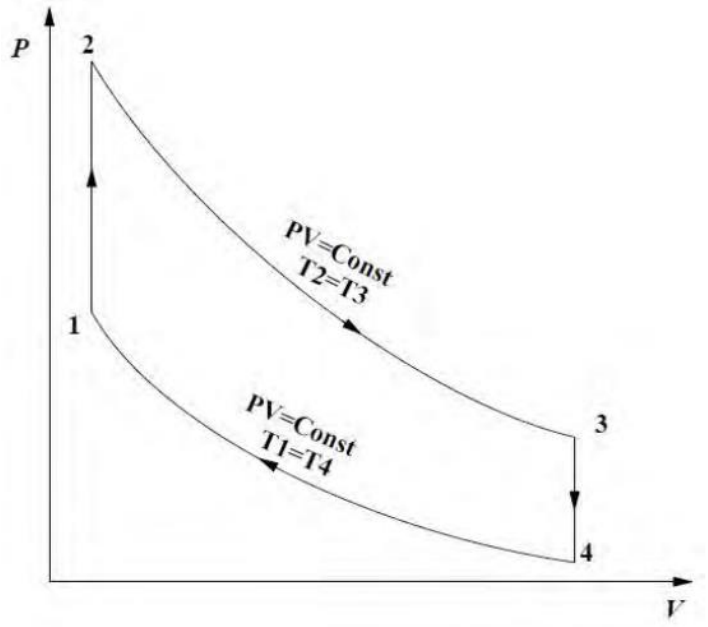

Figure 1.5: Stirling Cycle P-V Diagram

In the P-V diagram, the path of the engine is represented by following four ideal curves, which are illustrated in Figure 1.5, tracing a sequence from point $1 \rightarrow 2 \rightarrow 3 \rightarrow 4 \rightarrow 1$.

The Stirling Generator emerges as a pivotal solution in the transition towards renewable energy, boasting diverse deployment options, dual-energy outputs, minimal maintenance demands, a design conducive to local production, and unprecedented cost-efficiency in energy storage and output.

The Stirling Generator finds applicability across various deployment scenarios, making it an ideal choice for:

- Businesses in need of both thermal and electrical energy
- Businesses requiring either thermal or electrical energy
- Small to large Combined Heat and Power plants, serving as a primary base generator, backup source, or stabilizing system
- Flexible storage solutions for boiler plants, ensuring consistent and optimal boiler capacity output
- Replacement of peak plant assets for both thermal and electrical energy generation
- Utilization as Distributed Energy Resources, aiding in distributed grid stabilization
- Complete integrated power plants for remote communities or businesses without access to the main grid supply
- Harnessing and redistributing curtailed renewable energy during periods of high demand

System Design

Eutectic Salt Selection

A latent heat-based Thermal Energy Storage (TES) system, compared to a sensible heat-based one, exhibits higher specific weight and volume. This unique characteristic enhances its suitability for integration within a Stirling dish system. In the realm of Phase Change Materials (PCMs), a promising option includes eutectic mixtures of alkali halides, possessing properties highly favorable for Thermal Energy Storage applications. The primary criterion for selecting a PCM revolves around its melting temperature aligning within the intended operational temperature range.

In the context of a designed system utilizing a 3-kW free-piston Stirling engine, the ideal PCM should possess a melting point ranging between 600 and 700°C. This specific range ensures the supply of energy to the engine at the necessary temperature, optimizing the system for peak efficiency. The NaF–NaCl eutectic mixture, comprising 34% mol. NaF and with a melting point of 680°C, emerged as the chosen PCM. This selection empowers the Stirling engine to sustain prolonged operation by leveraging the latent heat of fusion near the material's melting point.

Furthermore, the system achieves the extraction of comparable amounts of solid and liquid sensible energy across an extended operational span, roughly between 750–300°C. Despite a potential decrease in the Stirling converter's conversion efficiency at lower temperatures, the system's capacity to consistently generate useful electricity remains intact. This resilience can be attributed to the remarkable turn-down ratio characteristic of Stirling engine generators.

The concentrator designated for this project boasts an effective surface area measuring 14.8 m², capable of providing an estimated 12.58 kW of solar energy to the system under an assumption of 850 W/m² direct normalized insolation (DNI). This robust energy input aligns with the system's design parameters, ensuring a substantial power supply for operational efficiency.

Single Tank with Filler Material

Thermocline-filler storage (TFS), a widely known concept, utilizes different densities to maintain the separation of salt volumes in layers. It involves a stratification technique and incorporates a packed bed of low-cost solid filler material, replacing around 50-75% of the molten salt. A protype was constructed and tested in 2002, offering a storage capacity of 688 MWh, operating at a maximum temperature of 400 °C.

In the charging phase, hot salt is injected into the storage tank from the top, while cold salt is removed from the bottom. Heat transfer occurs between the molten salt and the solid filler material within the packed bed, where a heat front moves from top to bottom through the bed (as depicted in Figure 1.6). Discharging operates in reverse.

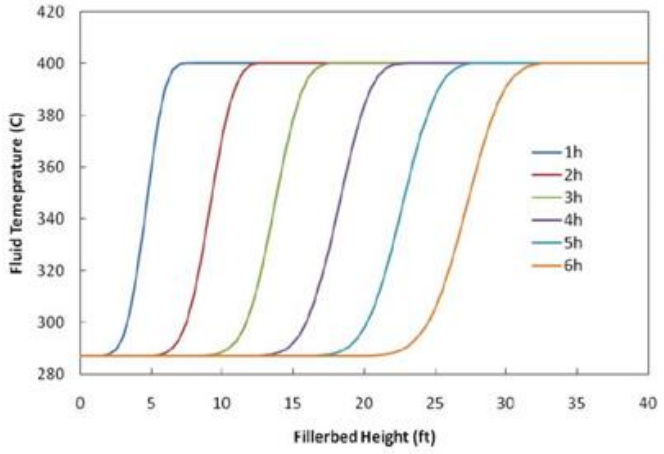

Figure 1.6: Simulated fluid temperature distribution in a TFS over the filler bed height (Ref. 4)

An estimated cost reduction potential of 20% to 37%, dependent on storage size, storage type, and solar thermal power plant technology is expected. Advancing TFS development at temperatures up to 560 °C addresses critical points including:

i. Research and characterization of filler materials with respect to thermodynamic properties, chemical stability in molten salt, and mechanical properties in packed bed applications.
ii. Optimization of filler material parameters, such as porosity and particle size, impacting pressure losses, heat transfer, and storage capacity.
iii. Validation of thermo-mechanical and thermodynamic models through tests on a representative scale to confirm simulation-derived results.
iv. Lack of operational experience above 400 °C demands prototype operation experience for temperatures up to 760 °C.
v. Investigation of thermal ratcheting effects and possible structural reinforcement to prevent container failure due to thermal cycling stresses.
vi. Research and qualification of components operating at higher temperatures for potential cost reduction in molten salt systems.

The advancement and resolution of these issues represent significant steps towards the practical implementation and optimization of TFS for commercial applications.

TES Module

The module encompasses a storage tank designed with an upper boiler dish, allowing for versatility in conducting various test setups. To validate simulation outcomes, multiple layers of thermocouples are positioned within the packed bed to monitor temperature distributions with precision.

The testing on this facility begins by focusing on the TFS storage concept. In this initial phase, the packed bed, consisting of filler material, is installed in three additional containers stacked within the tank. This setup enables the exploration of different materials, various packed bed arrangements, and diverse measurement configurations.

For the charging and discharging processes, the tank is linked to two supply tanks operating at different temperature levels. While these supply tanks are dedicated solely for testing purposes, they are not required in an actual system. As outlined in Table 1.2, temperature levels within the design limits can be flexibly chosen to meet the needs of specific tests.

Figure 1.7 illustrates a simplified scheme of the sub-facilities, depicting the storage on the left and the component on the right. The process for discharging involves pumping colder salt from the blue tank into the bottom of the storage tank while an equal amount of salt is returned through a level drain. Conversely, during the charging process, hot molten salt is pumped from the red tank to the top of the storage tank, simultaneously withdrawing salt from the bottom and returning it to the blue tank. This setup allows for maintaining consistent test conditions.

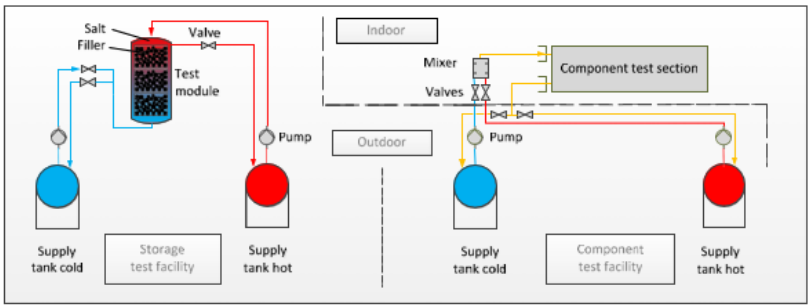

Figure 1.7: Simplified Schematic - Sub-Facilities (Ref. 4)

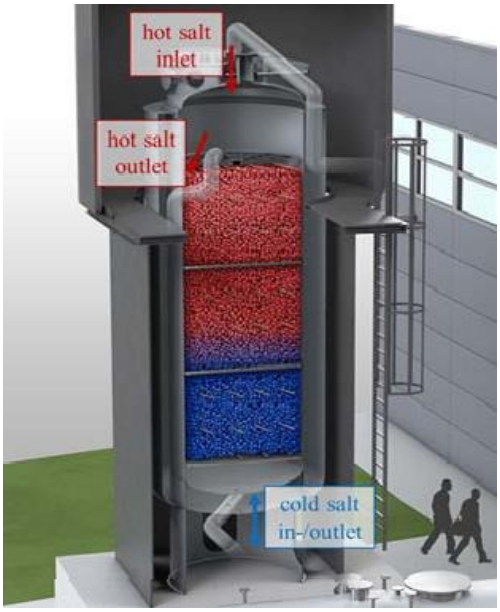

Figure 1.8: TFS Module (Ref. 4)

To ensure stable temperatures within the salt inventory despite variations in return temperatures, the supply tanks are outfitted with a cooler (blue tank) and an electric heater (red tank). This setup maintains the salt at a constant temperature level throughout the testing process (Figure 1.8)

Sub-facility	Storage test facility	Component test facility Molten salt
medium	Nitrate-Nitrite salt mixtures	Nitrate-Nitrite salt mixtures
Min. operation temperature	150 °C	150 °C
Max. operation temperature	760 °C	760 °C
Max. mass flow rate	4 kg/s	8 kg/s
Max. mass of filler material	45 t	n/a
Max. salt storage volume (without filler material)	22 m³	n/a
Max. thermal gradient at the test section inlet	n/a	50 K/s

Table 1.2: Summary of TES Test Facility Characteristics (Ref. 4)

TES Module Support

The TES container was affixed to a support ring, securely joined to the Stirling engine heater head via welding and brazing techniques. For optimal TES support, the design employed flexure springs, engineered to permit axial compliance for casing movement and thermal expansion while maintaining lateral rigidity to prevent gravitational sagging effects.

In this specific structural configuration, the flexures were directly connected to the TES container, leading to a notable thermal gradient across the flexure. Acknowledging the potential for elevated thermal stresses resulting from this setup, a meticulous optimization process was undertaken. This optimization ensured that the flexures operated within the material endurance limit, effectively mitigating excessive thermal stress.

The detailed intricacies of the TES flexure design process have been extensively discussed by the authors in a separate paper, offering a comprehensive insight into this aspect of the system. The distribution of temperatures and stress fields characteristic of this design approach is visually depicted in Figure 1.9, presenting a snapshot of the thermal and stress landscape within the system.

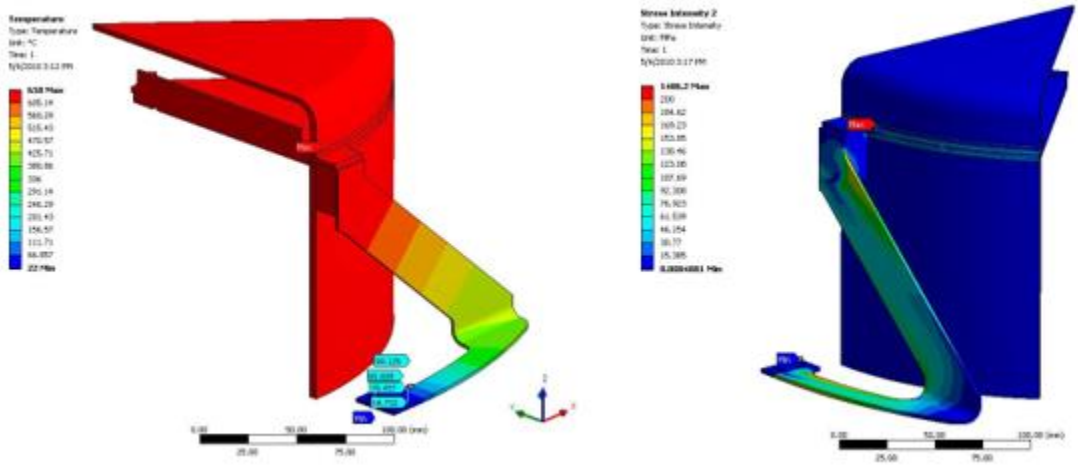

Figure 1.9: Temperature distribution (left) and stress field (right) within the designed thermal energy storage (TES) flexure (Ref. 5)

TES Module Design

The prototype features a Thermal Energy Storage (TES) free-piston Stirling engine, as showcased in Figure 1.9. This 3-kW engine utilizes its heater head as the primary heat pipe's condenser, facilitating the transfer of incoming solar energy to both the Stirling engine and the PCM storage material. Within this system, secondary heat pipes are intricately embedded into the NaF–NaCl eutectic PCM salt.

Comprising several essential components, the system includes a receiver vapor chamber, serving as the evaporator for the central primary heat pipe. Additionally, it encompasses the TES container, the supporting flexures for the Stirling engine, and the flexure support frames, all crucial for structural integrity and operational efficiency.

The Stirling engine and the linear alternator showcase specific dimensions, with a diameter of 203 mm and 260 mm, respectively. When combined, these components form an assembly with a total length of 533 mm. Meanwhile, the TES module itself measures 424 mm in length and possesses a diameter of 300 mm, highlighting its substantial physical presence within the system's configuration.

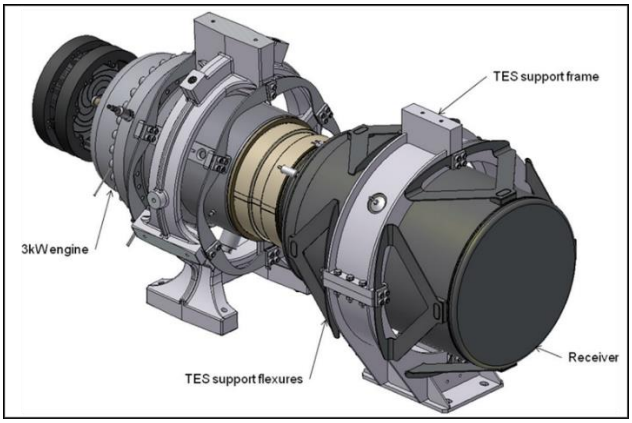

Figure 1.10: Stirling engine and TES module assembly (Ref. 5)

Figure 1.10 presents a detailed schematic of the Thermal Energy Storage (TES) module, illustrating the processes involved in both charging and discharging. Within this schematic representation, the yellow area signifies the heat pipe working fluid, while the gray color indicates the NaF–NaCl PCM. Red arrows denote the directional flow of heat.

During the charging phase, solar energy is absorbed by the TES receiver's surface, located on the left side of Figure 1.11. This absorption induces the evaporation of sodium within the heat pipe, positioned in contact with the receiver. The vaporized sodium migrates towards the Stirling engine's heater head or heat acceptor, situated on the right side of Figure 1.11. Subsequently, the sodium condenses, effecting the transfer of thermal energy to both the Stirling engine and the PCM. Notably, the Stirling engine primarily absorbs the bulk of the incoming thermal energy, while any surplus heat is directed to the PCM through an array of 32 embedded heat pipes, each having a 12.7 mm diameter.

Conversely, during the discharging phase, the stored energy within the PCM is extracted and transferred to the Stirling engine via secondary heat pipes, as depicted in Figure 1.11 In this discharging mode, the secondary heat pipes operate as the evaporator, whereas during the charging phase, they function as the condenser section. This delineation of roles between charging and discharging ensures the effective management and transfer of thermal energy within the Stirling Engine.

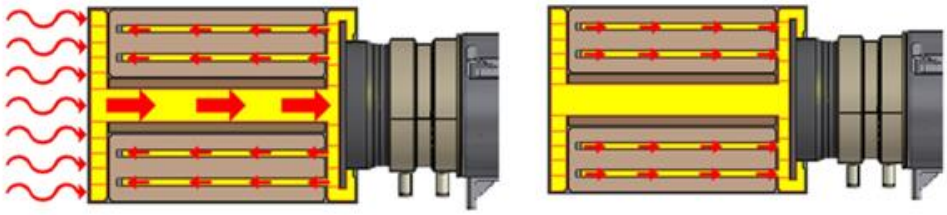

Figure 1.11: TES module schematic for charging (left) and discharging (right) mode (Ref. 5)

A comprehensive design analysis of the Thermal Energy Storage (TES) module was diligently carried out prior to the commencement of testing. This involved a meticulous determination of the heat transfer limit, aligning with the designated operational temperature. The capillary pressure limit of the wick and the sonic limit of the vapor in a pipe were pivotal factors in establishing this heat transfer threshold.

During the on-sun operational phase, the concentrator dish supplies a nominal heat rate of approximately 12 kW. This thermal energy is dispersed over the 30 cm diameter evaporator receiver surface, optimizing the heat absorption process.

Notably, the design analysis scrutinized several limiting scenarios during the wick evaluation:

1) Gravity-Neutral Horizontal Charging (Figure 1.12a): Investigating scenarios where gravity has a negligible effect on the charging process.
2) Mid-day Vertical Charging (Figure 1.12b): Assessing adverse gravity conditions for the secondary heat pipe but gravitational assistance for the primary heat pipe during mid-day charging.
3) Gravity-Aided Operation of Secondary Heat Pipes During Discharging (Figure 1.12c): Examining the scenario where the secondary heat pipes operate under gravitational assistance during discharging, specifically with the dish pointing downward.

These investigations into diverse operational orientations and gravitational effects provide crucial insights into the TES module's performance under varied conditions, ensuring a robust and adaptable design to handle different operational scenarios effectively.

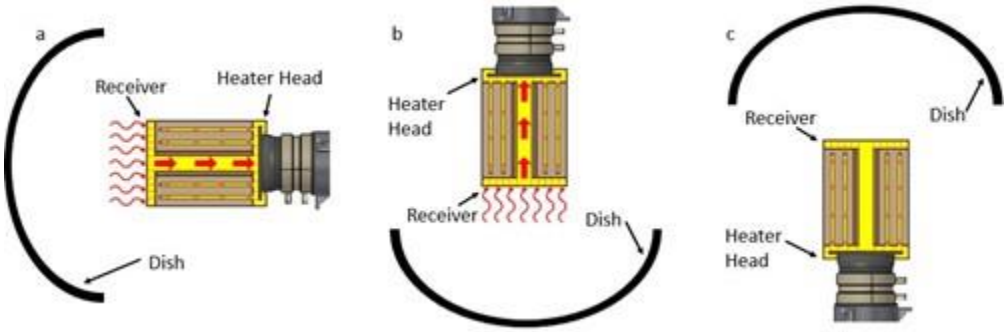

Figure 1.12: TES module orientations studied: (a) gravity-neutral horizontal charging; (b) mid-day vertical charging (adverse gravity for the secondary heat pipes and gravity-aided for the primary heat pipe), and (c) gravity aided discharging of the secondary heat pipes with the dish pointing downwards (Ref. 5)

The examination of the gravity-neutral charging scenario revealed that the capillary pressure suffices for the condensed sodium to re-enter the heat pipes effectively. In the mid-day operational mode, the vertical orientation of the module facilitates the return of the condensed sodium to the primary heat pipe evaporator through gravitational assistance, obviating the necessity for wicking in this context.

However, within the secondary heat pipes, a distinct challenge arises. The condensate within these pipes must traverse their entire length against the force of gravity to reach the central heat pipe and subsequently the primary evaporator. The finite element method (FEM) analysis, represented in Figure 1.13, specifically focusing on the heat pipe array, revealed a required maximum capillary pressure of 2140 Pa. This value was compared to the available 3100 Pa offered by the selected wick. Consequently, it was determined that the secondary heat pipes would effectively operate even under such extreme orientation, given that their functionality aligns with the available capillary pressure.

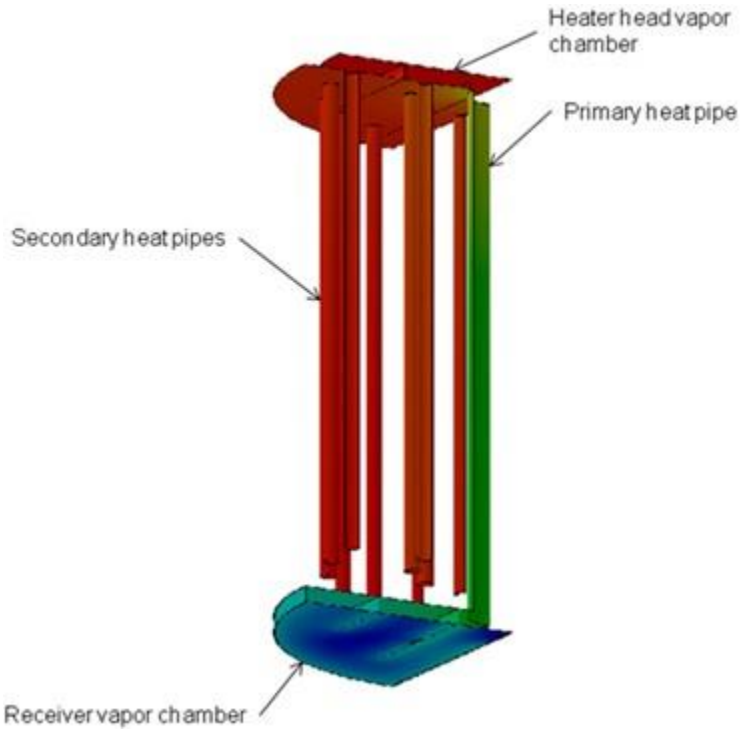

Figure 1.13: Wick finite element method (FEM) analysis (Ref 5)

During the discharging phase, both the Stirling engine and TES module will be vertically oriented, but with a distinctive alignment where the dish is directed towards the ground, allowing the Phase Change Material (PCM) to solidify and contract (as shown in Figure 1.12c). This orientation facilitates the formation of voids near the receiver end, while the secondary heat pipes once again operate against adverse gravity conditions.

The structural integrity of the TES container underwent a meticulous analysis, primarily focusing on the cold startup scenario, where the engine initiates electricity generation in the morning. At the outset, both the entire TES structure and the PCM are at ambient temperature. As the receiver receives direct sunlight, its temperature rises swiftly, inducing thermal expansion and generating significant thermal stresses.

In a worst-case scenario simulated for temperature distribution within the Stirling Engine, a temperature of 650°C was applied to the TES vessel, while the flexure attachments were maintained at 22°C. Additionally, assumptions were made regarding the 3-kW engine temperature at 22°C, with a thermal gradient along the heater head. These conditions were designed to represent the most extreme circumstances for temperature distribution within the system.

The temperature field of the integrated TES and engine is illustrated in Figure 1.14, capturing the thermal load and the system's orientation. Furthermore, the stress analysis, considering both the thermal expansion effects and the combined weight of the engine and TES module when the system is oriented horizontally, demonstrated that the stress ranges are well within the design limits allowable for the TES and Stirling engine materials. These allowable stress ranges adhere to the standards outlined in the ASME pressure vessel code. The contour plot in Figure 1.15 provides a visual representation of the stress distribution across the system.

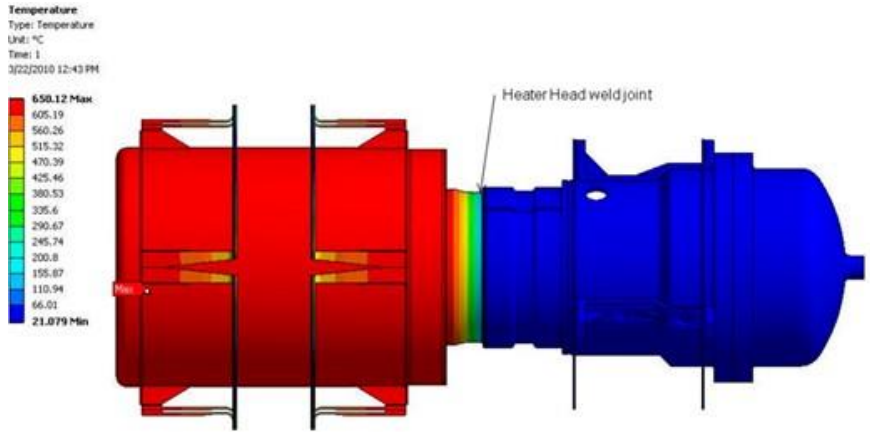

Figure 1.14: Temperature Field in Engine/ Stirling Engine (Ref. 5)

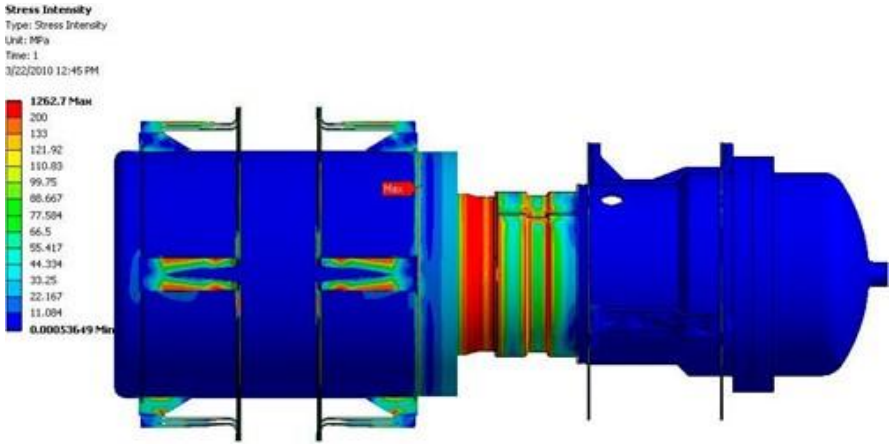

Figure 1.15: Stress distribution in engine/ Stirling Engine (Ref. 5)

The stress analysis results have formed the cornerstone for developing a system control algorithm, enabling the modulation of the heating rate directed to the receiver to maintain material stresses below their defined limits. Strategically placed thermocouples on the surface of the TES module continuously record real-time temperatures. These temperature readings are monitored and employed within the control algorithm.

The thermal loading on the TES vessel underwent comprehensive examination using Ansys structural models to explore the impact of different heating rates on the stress field within the structure. A series of transient analyses were conducted, recording temperatures at specific probe locations alongside the resulting stresses.

Furthermore, extensive laboratory tests validated the efficacy of managing thermal stresses induced during a cold startup phase. These tests confirmed that by employing temperature measurements and adjusting the heating rate to the receiver using the established protocols, the system effectively mitigates and controls the impact of thermal stresses.

Overall, the integration of a robust system control algorithm and real-time temperature monitoring, coupled with precise adjustments in the heating rate, effectively safeguards the structure against thermal stress, ensuring optimal and safe operation during various operational phases, especially during cold startups.

Assembly & Verification

Once the core engine components were manufactured, assembly and validation procedures were conducted to ensure high-level functionality. During this phase, the assembly process for the generator was tested and refined, resulting in a significantly streamlined procedure with minor component modifications.

Essentially, the assembly involved integrating the crankshaft and piston components around the cold-side steel plate, establishing it as the foundational structure for the entire engine. Subsequently, the heat exchanger and regenerator components were assembled, and the engine was enclosed within its containment shell, then externally insulated. The assembly process continued with the alternator; the rotor magnet discs were initially coupled on both sides of the stator, followed by connecting the rotor to the crankshaft and attaching the stator to the cold-side steel plate. Finally, the engine was placed into the pressure vessel.

Transducer Alternator Model Tuning

Modeling a linear alternator is straightforward, necessitating only three components. However, it comes with limitations as it overlooks crucial physical phenomena and possible losses such as eddy currents, hysteresis, and flux leakage. Moreover, it mandates that the user possesses data to input properties like alternator inductance, resistance, and the motor constant Ki.

For the ASC, values for alternator inductance and resistance are established. To address losses, an additional resistor RLOSS is introduced in the Sage model, assuming losses are directly proportional to current. Determining the suitable resistive loss isn't simple, given that real losses might vary with the converter's operational point. The same complexity could hold true for Ki, as its behavior might also change under different operational conditions.

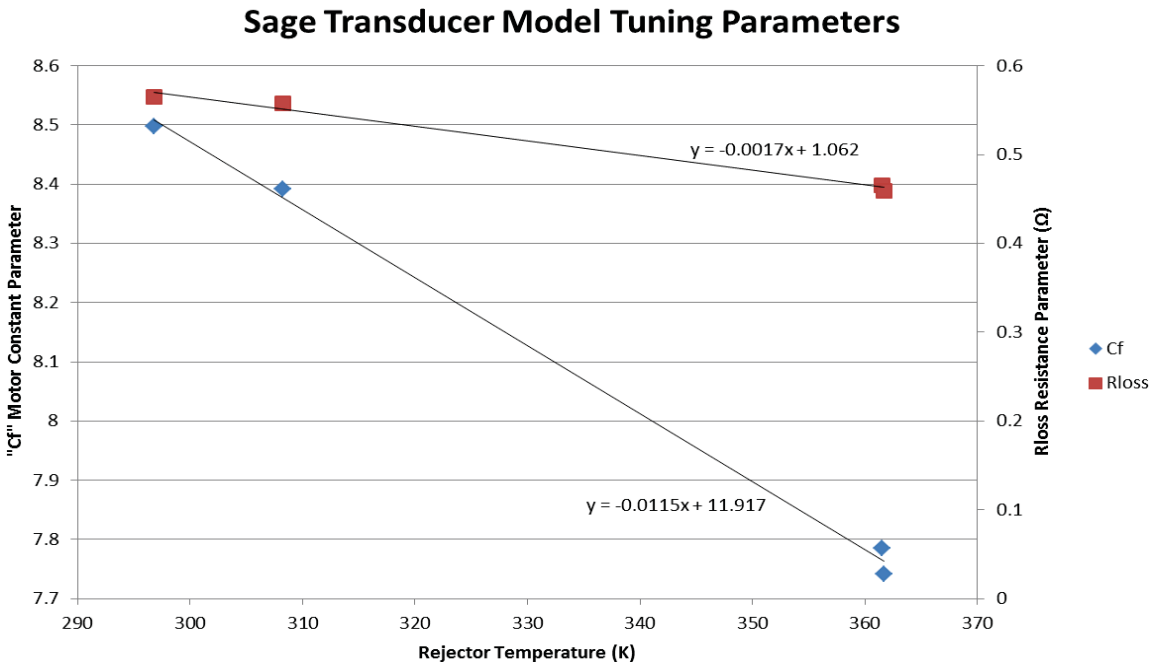

Figure 2.1: Transducer tuning parameter value as a function of rejector temperature (Ref. 6)

Utilizing the Sage optimization tool proves instrumental in exploring suitable values for Rloss and Ki. An estimated value for both parameters can be initially entered into Sage and designated as optimization variables. Output variables are constrained, and an objective function is formulated for Sage to attain by altering Rloss and Ki values. This optimization is based on performance data from the ASC, with stringent constraints on current and voltage output values to align within 2.5 percent of the measured data. The objective is to match the measured power factor.

This optimization exercise was conducted across four distinct operational points of the ASC: the beginning of mission (BOM) and end of mission (EOM), encompassing high reject (HR) and low reject (LR) temperatures for each case. The outcomes revealed slight variations in Rloss and Ki values among the operational points, with a discernible correlation noted between Ki and rejection temperature (Figure 2.1). Notably, this correlation aligns with the understanding that the transducer and Rloss components do not account for performance changes due to temperature variations. Leveraging this correlation, Ki values were input into Sage as a function of rejection temperature, and the simulation was repeated across the test points.

The assessment of the engine's thermal performance was extensive, albeit excluding the hot-side external fluid-to-metal component. However, the characterization of the cold side serves as a reliable approximation, as identical equations are employed in both side designs, ensuring validation of the entire system.

Sage Linear Alternator Modeling with Electromagnetic Components

Developing a linear alternator model integrating electromagnetic (EM) components is considerably more intricate compared to the simpler "transducer model." However, this approach offers the distinct advantage of capturing the system's physical characteristics from fundamental principles. In the Sage environment, the high-level EM components employed to model the linear alternator encompass a two-pole magnetic gap, a wire coil, ferromagnetic cores, and magnetic reference and connection blocks. These components are designed with the requisite magnetic flux boundary interfaces and interconnected as illustrated in Figure 2.2.

It's crucial to note that the visual representation of component layout in Sage might not directly resemble a linear alternator. Understanding the underlying physics that Sage attempts to simulate is key, considering that the components within Sage are structured to replicate the electromagnetic behaviors and interactions essential to model a linear alternator accurately.

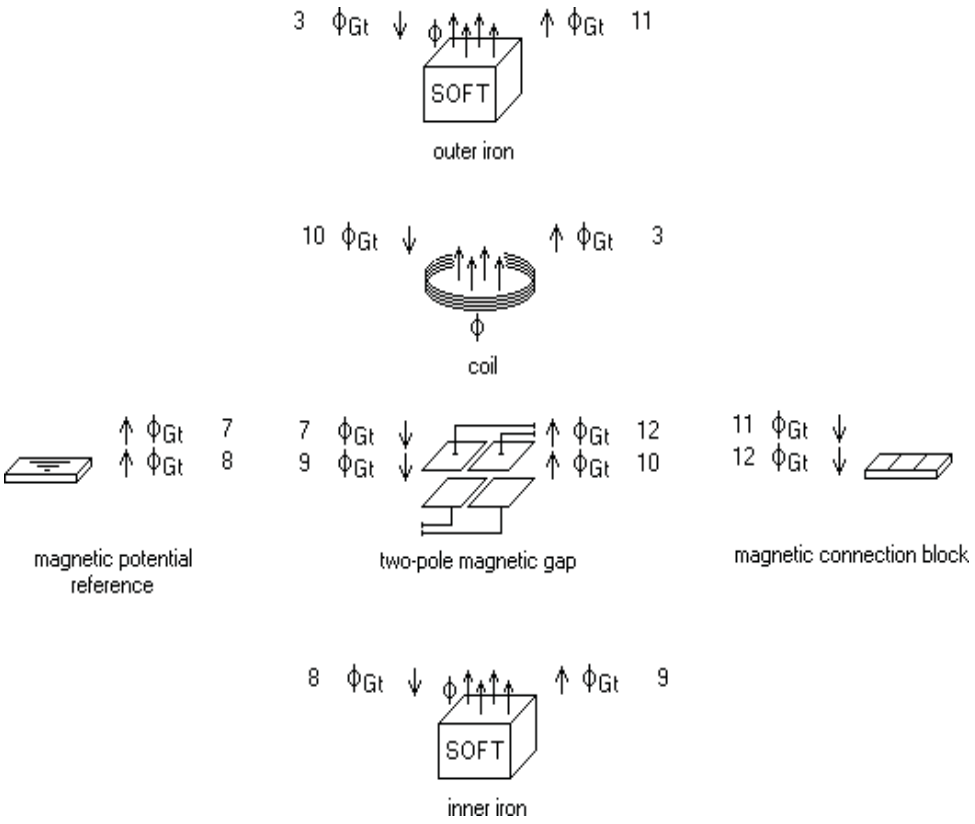

Figure 2.2: Sage linear alternator high-level components (Ref. 6)

Sage Electromagnetic Model Connections and Solution Method

The Sage electromagnetic model interconnects various magnetic components such as permanent magnets, magnetic poles or gaps, and ferromagnetic materials through magnetic flux boundary interfaces, which are contingent upon the magnetic potential difference (or magnetomotive force) across each component. Each component establishes the correlation between magnetic flux and magnetomotive force based on its specific magnetic properties. For instance, the wire coil component features both current and magnetic flux connections, while the magnetic pole components have force and magnetic flux connections. This comprehensive arrangement facilitates the modeling of energy conversion from mechanical to electromagnetic and supports the holistic modeling of the converter.

The Sage solution framework for electromagnetic models operates on a magnetic circuit approach. If the magnetic flux in a system follows a well-defined path, the system can be understood as a magnetic circuit, similar to current confined to wires and components in electric circuits. Table 2 enumerates the primary magnetic properties alongside their corresponding electric properties in analogy.

In the magnetic circuit analogy, the magnetic system can be depicted as an electric circuit. Figure 2.3 illustrates an electromagnetic system and its corresponding electric circuit. For instance, the coil generates the magnetomotive force F, and a magnetic flux Φ "circulates" through the system. It's important to note that "circulation" is a continuation of the electric circuit analogy—similar to current flow in an

electrical circuit—although nothing physically flows through the magnetic system. The reluctance in the magnetic system due to the ferromagnetic core and air gap are likened to resistors in an electric circuit.

With this analogy, the system model can be solved using Equation 2.1 (Ref. 6), which corresponds to Ohm's law, allowing for a coherent understanding of the system's behavior and interactions within the Sage electromagnetic model.

$$\mathfrak{F}=cp\mathfrak{R}$$

Equation 2.1

Magnetic Property	Electric Property
$\mathfrak{F}$ = Magnetomotive force (mmf) (amp-turns)	V = Electromotive force (emf) (V)
cp = Magnetic flux (Wb)	I = Electric current (A)
$\mathfrak{R}$ = Magnetic reluctance (H^{-1})	R = Electric resistance (0.)
μ = Permeability	cr = Conductivity

Table 2: Magnetic and Electric Analogous Terms (Ref. 6)

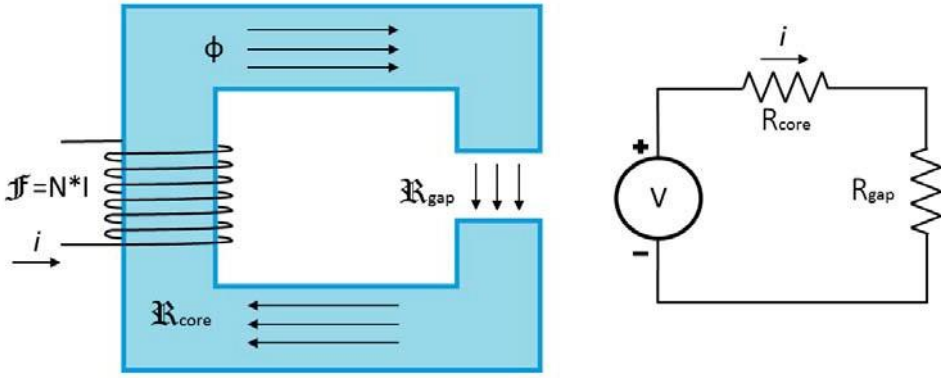

Figure 2.3: Magnetic Circuit Analogy (Ref. 6)

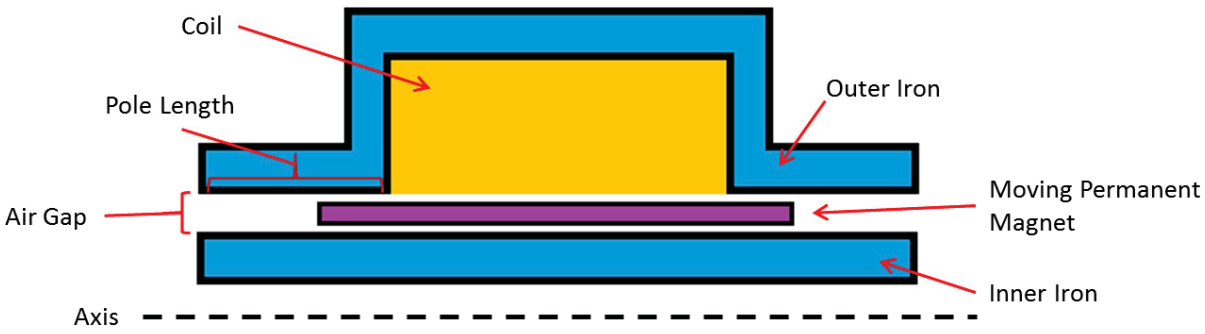

Figure 2.4: Linear Alternator Generic Two-Dimensional Cross Section Assumed by Sage (Ref. 6)

Properties of Sage Electromagnetic Components and Subcomponents

The input properties of Sage EM components are structured around the fundamental geometry of the alternator and the interrelationships between its components. Figure 2.4 presents the assumed generic axisymmetric structure in the Sage alternator model. The two-pole magnetic gap component sets the overall framework of the alternator, defining parameters such as pole length, the separation between poles (directed along the axis), and the magnetic gap between pole faces (directed perpendicular to the axis). Subcomponents within the two-pole component include an "EM container," capable of accommodating PM or ferromagnetic elements, catering to various types of magnetic systems, such as moving magnet or moving iron. These subcomponents model the magnetic material, dimensions, and initial conditions like temperature and position. Alongside the magnetic flux interfaces generated from the magnetic poles, there's a force interface connecting the magnet (EM container) to the force interface of the piston.

The inner and outer iron components in the model are contingent upon the ferromagnetic material employed for the alternator core, considering its effective magnetic path length and area. The coil component encapsulates the physical parameters of the coil wire, such as the number of turns, wire cross-sectional area, coil cross-sectional area, and coil average diameter. Coil resistance is an output parameter derived from calculations involving wire dimensions, material properties, and temperature. The coil inductance is also an output parameter, calculated (as per Equation 2.1) rather than being an input. The inductance is shown to be dictated by the physical dimensions of the coil and the magnetic properties of the iron core. In the case of the alternator, where the coil area remains constant, the magnetic flux linkage can be simplified using Equation 2.2 (Ref. 6), where "A" represents the area of the coil and "l" signifies the length of the coil. Subsequently, the inductance of the alternator can be defined by its physical properties through Equation 2.3 (Ref. 6), based on its initial definition. This approach enables a detailed understanding of the alternator's inductance in relation to its physical attributes.

$$\text{f ł ù} = \frac{\mu N^2 A}{l} I$$

Equation 2.2

Equation 2.3

$$L = \frac{dcp}{di} = \frac{\mu N^2 A}{l}$$

Sage Electromagnetic Material Properties

In the Sage EM library, various ferromagnetic and permanent magnet (PM) materials are available, each with typical material properties. These properties can be adjusted or new materials added to meet the specific requirements of the model. How material properties are defined in Sage and the assumptions made about these materials play a crucial role in the model's overall performance.

PM material properties are characterized by their intrinsic (J(H)) and normal (B(H)) demagnetization curves, as depicted in Figure 2.5. In these curves, J represents magnet polarization (in tesla, SI unit), B signifies magnetic flux density (in tesla, SI unit), and H refers to magnetizing force (in amperes per meter, SI unit). Sage utilizes the endpoints of the J(H) curve (residual magnetic flux, Br, and magnetization coercive force, Hcj) as inputs and incorporates a curve fitting term to match the demagnetization bend.

Magnetic characteristics inherently exhibit temperature dependency, so Sage permits inputs at multiple temperature points and otherwise assumes a linear relationship based on the Curie temperature.

The ability to define and adjust these material properties within Sage is fundamental to accurately capturing the behavior of the materials under varying conditions, ensuring the model reflects real-world performance and characteristics of the electromagnetic system being studied.

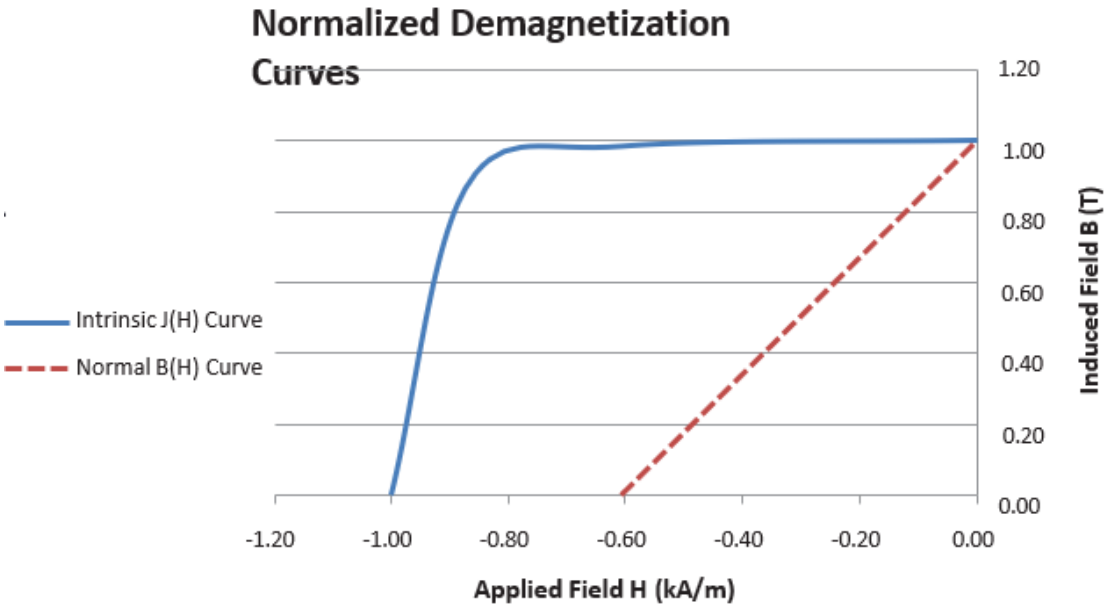

Figure 2.5: Permanent magnet demagnetization curves (second quadrant of hysteresis loop) (Ref. 6)

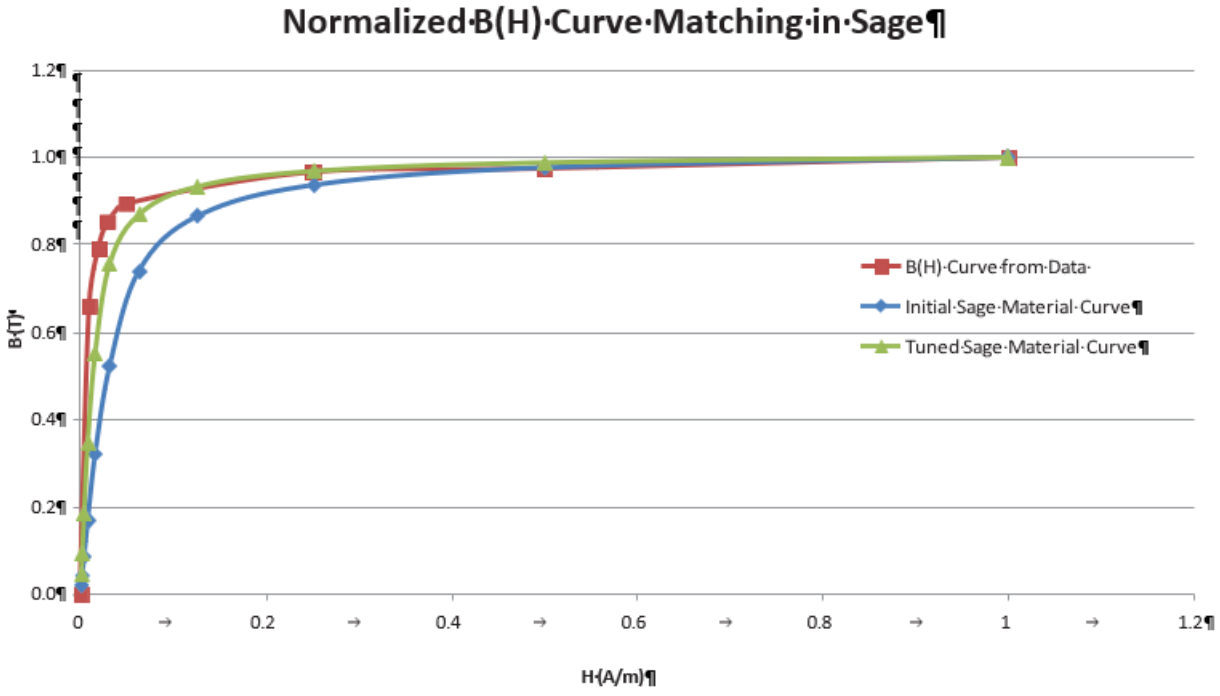

Figure 2.6: B(H) curve matching in Sage for ferromagnetic core material (Ref. 6)

In Sage, the definition of ferromagnetic material properties mirrors that of permanent magnet materials, relying on critical points of the J(H) curve specific to the material. These points include the saturation magnetic polarization (JSat, measured in tesla, SI unit) and the induction coercive force (measured in amperes per meter, SI units), which are input at a designated temperature. If available, data points for multiple temperatures can be input; otherwise, Sage assumes a linear decrease to zero at the Curie temperature. Additionally, the maximum relative permeability (μr) is specified for the material. Sage offers a ferromagnetic material B(H) mapping model, facilitating comparison and adjustment of the B(H) curve for the material. Figure 2.6 showcases a comparison between the B(H) curve derived from test data and the B(H) curve generated within Sage using available data. This comparative analysis enables the determination of a "tuned" value for μr and JSat, allowing alignment of the B(H) curve to match the test data. This approach enables fine-tuning of material properties within Sage to reflect the real-world characteristics of ferromagnetic materials, enhancing the accuracy and reliability of the electromagnetic model.

Sage Electromagnetic Alternator Model Tuning

The Sage alternator model functions as a one-dimensional representation, assuming symmetry along its axis. While this assumption generally performs well, it doesn't fully capture the reality of manufacturing and assembly, which might introduce non-symmetric aspects, such as the outer iron core laminations lacking continuous coverage. Additionally, the dimensions of the actual alternator, as depicted in the idealized Figure 2.4, are more intricate than represented. These discrepancies between the idealized model and actual geometry can lead to inaccuracies, potentially causing Sage to overestimate or underestimate parameters such as the quantity of iron core material, magnetic path length, and area.

Such discrepancies can affect the accuracy of the magnetic circuit model by modifying the magnetic reluctance of components or altering magnetic flux through components due to inaccurate area calculations.

Another potential error source in the electromagnetic (EM) model arises from magnetic fringe field effects across the magnetic gaps at the poles of the alternator. Fringing flux occurs at gaps in the ferromagnetic path, causing the magnetic field to expand outward. Sage models this fringing flux in a manner akin to an electric field in a parallel plate capacitor, leveraging the similarity in governing equations between the two phenomena. The study of fringe fields in capacitors provides a foundation for modeling these effects in the Sage framework.

It's plausible that not all windings of the alternator coil enclose an equal amount of magnetic flux, contrary to what Sage assumes. Figure 2.7 illustrates a two-dimensional flux plot through an alternator, generated using the Maxwell FEM software package, showcasing the presence of fringing fields and unevenly distributed field lines in the inner core along the coil windings due to the off-center positioning of the permanent magnet. This visual representation highlights the non-uniformity of the magnetic field within the alternator, which the one-dimensional Sage model might not fully encapsulate.

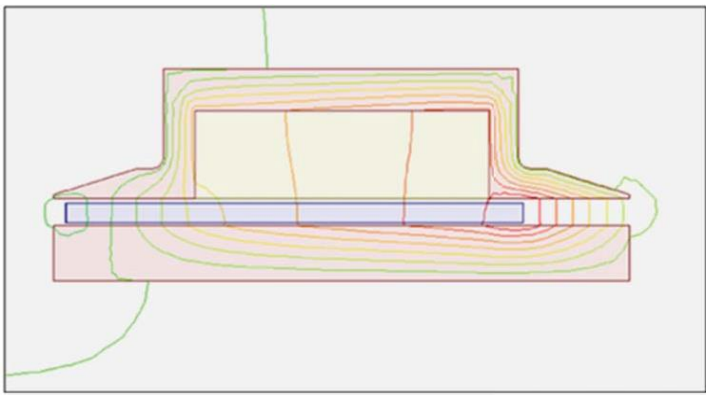

Figure 2.7: Two-dimensional magnetic flux plot of a linear alternator (Ref. 6)

Tuning Parameters

In Sage, there are specific built-in tuning parameters designed to address the recognized limitations within the electromagnetic (EM) components used for modeling. These parameters aim to refine the accuracy of the model based on real-world discrepancies. One such parameter is the "FringeMult," a multiplier that directly adjusts the impact of fringing fields at the magnetic poles in the model. This parameter enables scaling the influence of these fringe fields, acknowledging and compensating for the model's limitations in representing them accurately.

Another tuning parameter, the "Jmult," serves to scale the strength of the permanent magnet (PM). This adjustment accounts for potential demagnetization that might have occurred during the magnet's operational use or reflects real magnet strength values that deviate from the presented figures in the material data sheet. Together, these parameters not only address specific known limitations but also offer a means to correct or compensate for other modeling inaccuracies, such as idealized geometry or magnetic flux path representations.

Furthermore, during the tuning of the alternator model, certain parameters may be adjusted to counteract inherent inaccuracies. The overall magnetic path length and area of the alternator could be modified to align more closely with the effective area of the iron cores, which might not be accurately represented in the axisymmetric assumption. Another adjustable parameter is the airgap dimension (lgap), which denotes the distance between pole faces. Modifying this distance influences the magnetic reluctance within the magnetic circuit, as denoted in Equation 2.4 (Ref. 6), offering an opportunity to rectify or adjust the model to better match real-world conditions.

Equation 2.4

$$\Re = \frac{l_{gap}}{\mu A}$$

Alternator Model Inductance Test and Verification

The inductance of the alternator significantly influences its performance and is contingent upon the overall geometry of the coil and iron cores. To enhance confidence in the physical parameters of the Sage alternator model, testing and fine-tuning the model to match the measured inductance of the alternator is essential.

The coil parameters, encompassing the number of turns, resistance, and dimensions, are usually well-documented and accurately modeled. Therefore, the permeance (the inverse of reluctance) of the magnetic path often becomes the focus for tuning within the model.

To verify the inductance of the alternator model, a separate model mirroring the input parameters of the actual alternator was created. This model was configured with a current source connected to the alternator, while the piston remained stationary and the magnets were centered in the alternator. This setup aimed to replicate the inductance test conducted during the manufacturing process of the linear alternator. A substantial current was input into the model, and the inductance was recorded in the output listing provided by Sage.

This testing approach, simulating the inductance test under controlled conditions, allows for a comparison between the measured inductance and the reported inductance from the Sage model. Any disparities between the actual inductance and the model's output provide insights into areas that might need adjustment or fine-tuning, facilitating an alignment between the physical performance of the real alternator and the model representation within Sage.

Alternator Model Performance Tuning Using Maxwell Model Simulation

The performance of the Sage electromagnetic (EM) alternator model was put to the test through a comparison with a Maxwell Finite Element Method (FEM) model of the alternator. This comparative analysis served a dual purpose: it sought to evaluate the accuracy of the one-dimensional Sage EM model against the more detailed three-dimensional FEM model and to generate simulated alternator performance data for fine-tuning purposes, particularly in the absence of standalone alternator test data.

During this comparison, a primary tuning parameter under scrutiny was the "Jmult" term. This tuning involved reassessing and potentially readjusting this parameter in the Sage EM alternator model. The aim was to align the performance and characteristics of the Sage EM model more closely with the outcomes of the higher-fidelity Maxwell FEM model, enhancing the accuracy and reliability of the Sage model.

Subsequently, this tuning process underwent reevaluation within the integrated ASC (Alpha Stirling Convertor) model. The revised Sage EM alternator model was integrated with the Stirling engine model, and the Jmult term was further adjusted. This iterative process aimed to optimize the overall performance of the integrated system by fine-tuning the Sage EM alternator model within the broader context of the ASC, ensuring greater alignment between the simulated and real-world performance characteristics of the system.

Simulation Results and Model Validation

The Sage transducer model and electromagnetic (EM) model were integrated with the Alpha Stirling Convertor (ASC) model and finely tuned across four critical operating conditions: beginning of mission low reject (BOM-LR), beginning of mission high reject (BOM-HR), end of mission low reject (EOM-LR), and end of mission high reject (EOM-HR). Simulations utilizing these tuned models at these operating points were cross-referenced with measured data obtained from convertor verification testing conducted on the actual equipment.

Following the convertor verification testing, the position sensor affixed to the displacer was removed before the ASC underwent extended testing. This slight alteration affected the mass of the displacer, prompting a corresponding adjustment in the Sage model to reflect this change accurately. The adjusted displacer mass in the Sage model was modified, and simulations were carried out to compare against performance map tests conducted at a different testing location.

This comprehensive process of combining, tuning, and refining the Sage models within the context of the ASC, as well as adjusting parameters to reflect real-world changes in equipment configuration, allowed for a robust comparison

between simulation outputs and actual test data. These comparisons served to validate the accuracy and reliability of the Sage models in replicating the ASC's performance across varying operational conditions and configurations.

Sage Advanced Stirling Convertor With Transducer Alternator Model Results

Table 2.2 showcases the measured parameters, delineates the conditions at the beginning of mission (BOM) and end of mission (EOM), and outlines the percentage discrepancies between the simulated data generated by the fine-tuned Sage ASC incorporating the transducer alternator model and the actual measured data points. In each case, the piston amplitude was standardized as an input parameter. The model exhibits a close correspondence with the measured data, showing differences of 5 percent or less across the majority of parameters.

Test Parameters Sage Transducer Alternator Model	BOM-LR	BOM-HR	EOM-LR	EOM-HR
Net-heat input, Q (W)	2.29%	-2.14%	5.37%	-2.36%
Piston amplitude (mm)	0.00%	0.00%	0.00%	0.00%
Displacer amplitude (mm)	0.73%	1.30%	0.82%	0.85%
Displacer to piston phase (degree)	1.01%	0.11%	2.03%	0.38%
Piston to current phase (degree)	-0.11%	2.30%	-1.51%	1.92%
Terminal power (W)	-0.27%	0.38%	0.64%	-0.46%
Power factor	0.21%	-0.43%	0.25%	0.30%
Voltage rms (V)	-2.64%	-2.43%	-1.18%	-2.78%
Current rms (A)	2.08%	2.38%	2.01%	2.37%
Efficiency (%)	-2.51%	2.58%	-4.49%	1.95%

Table 2.2: Sage Transducer Model Percent Error to Test Data,

Beginning of Mission (BoM)/End of Mission (EoM) Point Comparison (Ref. 6)

The model underwent an update to account for the change in displacer mass, and subsequent simulations were conducted. These simulations were then compared to performance map data obtained from tests conducted at a different location. Notably, the amplitude in the test data was varied during these comparisons.

Sage Advanced Stirling Convertor With Electromagnetic Alternator Model Results

Table 2.3 exhibits the parameters measured at the beginning of mission (BOM) and end of mission (EOM) operating conditions, presenting the percentage error between the Sage ASC model with the electromagnetic (EM) alternator and the measured data. The acceptor and rejector temperatures were initially set as inputs, while the piston amplitude was aligned within a 0.05 percent match. After tuning at the BOM-LR operating conditions, the model demonstrated agreement with the measured data within a 2 percent discrepancy. Across the remaining operating points, the model aligned within a 6 percent margin or better.

Following an update to accommodate the change in displacer mass, simulations were conducted and compared to performance map data collected from a different location. The simulations ensured consistency with the acceptor and rejector input temperatures, as well as the piston amplitude.

Test Parameters Sage EM Alternator Model	BOM-LR	BOM-HR	EOM-LR	EOM-HR
Net-heat input, Q (W)	-1.03%	-5.07%	1.92%	-5.45%
Piston amplitude (mm)	0.00%	0.05%	-0.05%	-0.05%
Displacer amplitude (mm)	-1.40%	-0.92%	-1.36%	-1.56%
Displacer to piston phase (degree)	-0.89%	-1.26%	-0.02%	-0.94%

Piston to current phase (degree)	0.44%	1.87%	−0.80%	1.92%
Terminal power (W)	0.44%	−3.96%	3.92%	−4.72%
Power factor	0.46%	1.45%	−0.63%	3.43%
Voltage rms (V)	−0.85%	−5.02%	2.57%	−5.32%
Current rms (A)	0.89%	−1.75%	1.70%	−2.37%
Efficiency (%)	1.48%	1.16%	1.96%	0.77%

Table 2.3: Sage Electromagnetic (EM) Model and Beginning of Mission (BoM)/End of Mission (EoM) Point Comparison (Ref. 6)

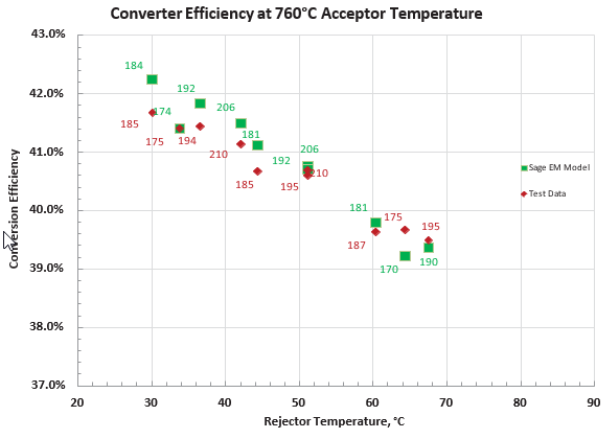

Figure 2.8: Sage Advanced Stirling Convertor (ASC) Model with Electromagnetic (EM) Alternator, Comparison of Efficiency (Ref. 6)

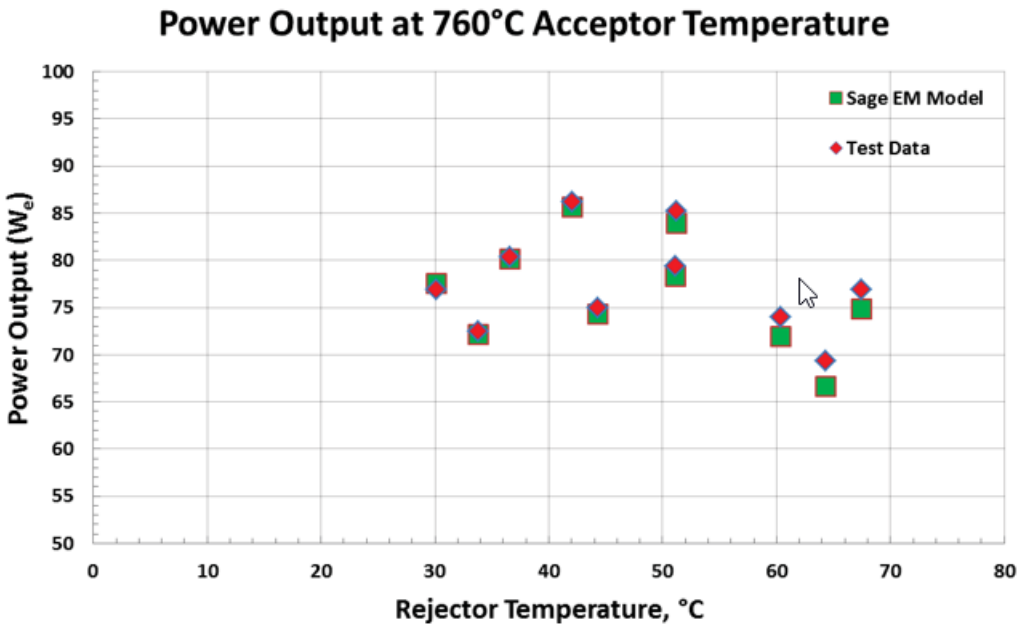

Figure 2.9: Sage Advanced Stirling Convertor (ASC) Model with Electromagnetic (EM) Alternator, Comparison of Power Output (Ref. 6)

Figure 2.9 illustrates the comparison between the power output of the electromagnetic (EM) model simulations and the corresponding test data. The model demonstrated good alignment with the test data at lower rejector (LR) temperatures. However, the disparity between the model and test data grows as the rejector temperature increases. This suggests that the model might not precisely consider temperature effects within the alternator, such as potential reductions in magnetic saturation within the iron core or diminished magnet strength as temperatures rise.

Despite this discrepancy, even at higher rejection temperatures, the model remained within a 5 percent margin of agreement with the test data. This indicates that while the model might not fully encompass temperature-related effects, it still performs reasonably well and accurately represents the system's behavior, especially within a reasonable margin of error.

Output Capacity with Tempature		Stirling Engine Operatting Tempature					
Desription	Currently Run at 70% Capacity	30.00 °C	37.00 °C	38.00 °C	42.00 °C	50.00 °C	50.00 °C2
Watts per Second	56.00 Watts per Second	80.00 Watts per Second	80.00 Watts per Second	86.00 Watts per Second	75.00 Watts per Second	80.00 Watts per Second	85.00 Watts per Second
Seconds in Min	60 Seconds	60 Seconds	60 Seconds	60 Seconds	60 Seconds	60 Seconds	60 Seconds
Killo Watts Per Second	3.36 KW per Second	4.80 KW per Second	4.80 KW per Second	5.16 KW per Second	4.50 KW per Second	4.80 KW per Second	5.10 KW per Second
Max KW Per Hour	201.60 kWh	288.00 kWh	288.00 kWh	309.60 kWh	270.00 kWh	288.00 kWh	306.00 kWh
MW Per day	4.84 MWh	6.91 MWh	6.91 MWh	7.43 MWh	6.48 MWh	6.91 MWh	7.34 MWh

Sage Alternator Model Comparison

In Figure 2.10, a comparison is depicted between the convertor efficiency of the Sage transducer model and the electromagnetic (EM) model of the alternator. This comparison showcases their default (untuned) configurations and their tuned setups when simulated at the beginning of mission (BOM) and end of mission (EOM) operating points. The default EM alternator model demonstrates better alignment with the data compared to the default transducer model, almost as closely as the tuned models.

A corresponding plot representing the comparison of power output (Figure 2.11) reflects similar outcomes. It's important to note that other parameters, such as voltage, current, and power factor, exhibit more significant variability in the default models, displaying discrepancies of up to 20 percent error in the untuned models. Despite these variations, the default EM alternator model remains relatively close to the data and compares favorably to the tuned configurations.

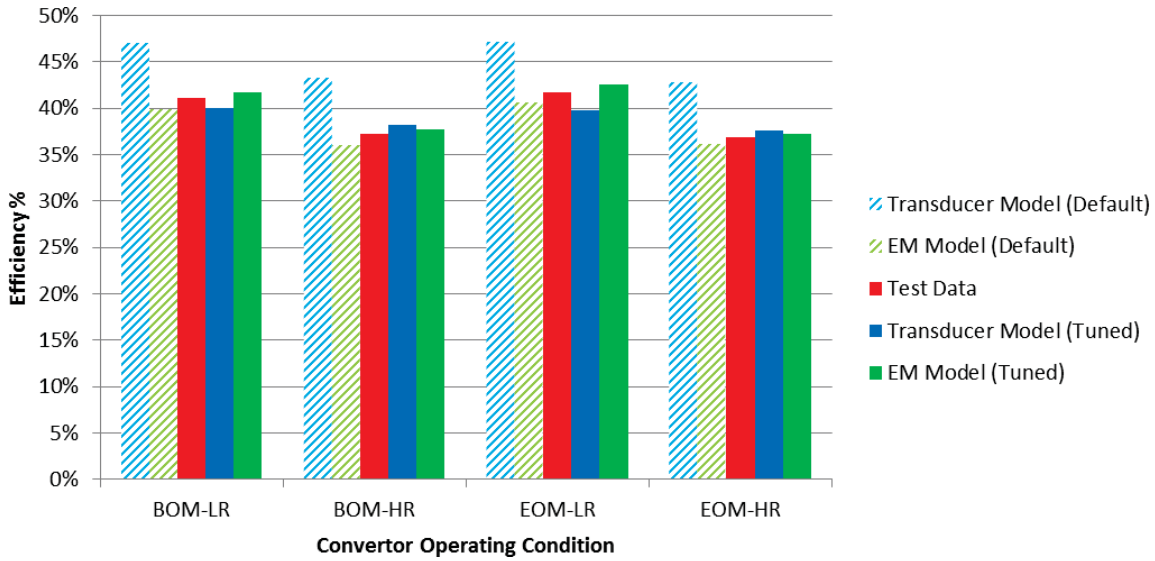

Figure 2.10: Sage alternator model convertor efficiency comparison (Ref. 6)

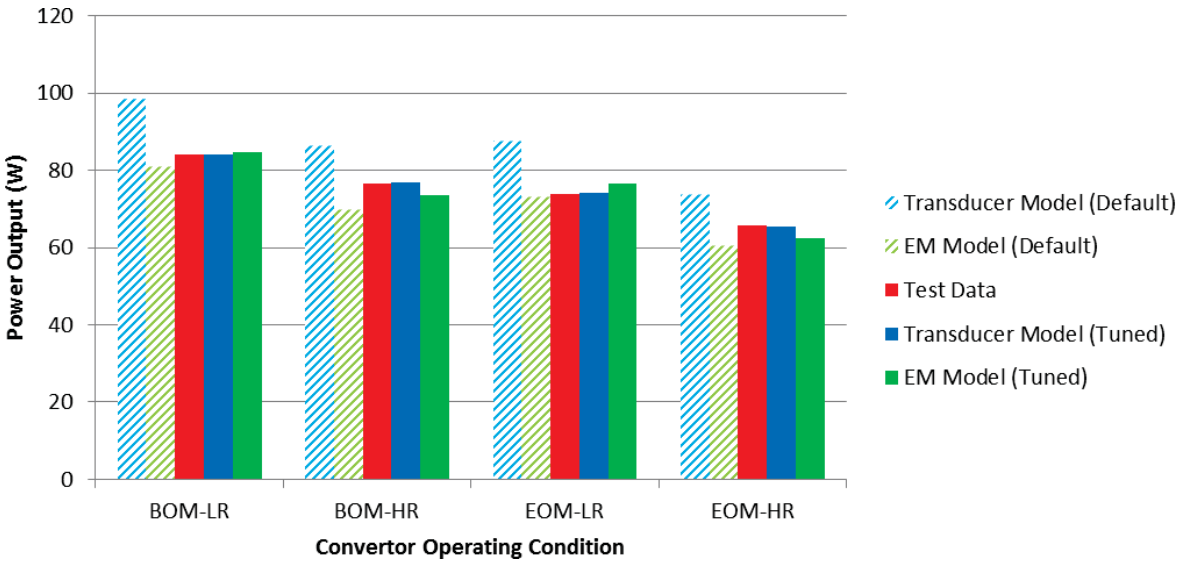

Figure 2.11: Sage alternator model convertor power output comparison (Ref. 6)

Materials and Methods

Basic Concepts of the Parabola and Earth–Sun Angles

The parabolic trough solar collector was constructed utilizing mirrors shaped in the form of a parabolic cylinder. These mirrors were specifically designed to reflect and concentrate solar radiation onto an absorber tube positioned along the focal line of the parabolic cylinder. At this focal line, the absorber tube captured the incoming solar radiation, converting it into thermal energy. Figure 3.1 illustrates a conceptual schematic showcasing the design and layout of the parabolic shape, outlining the components involved in this solar collection system.

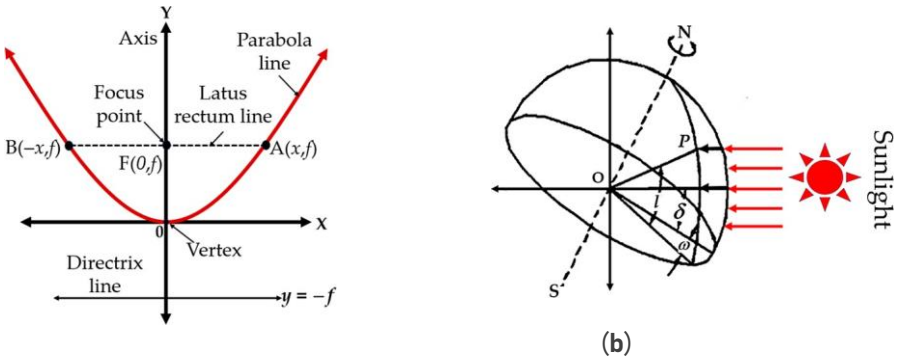

Figure 3.1: Basic concepts of (a) the parabola and (b) the Earth–Sun angles (Ref. 7)

The equation for the parabolic trough in cylindrical coordinates is shown below (Equation 3.1) (Ref. 7)

$$y = \frac{x^2}{4f}$$

Equation 3.1

The reflector of a suitable parabolic design typically has focal length (f) to aperture width (W) ratio of about 0.25 as calculated from the Equation 3.2 (Ref. 7)

$$\frac{f}{W} = 0.25$$

Equation 3.2

The geometric concentration ratio (*CR*) of the parabolic trough collector is calculated from the Equation 3.3 (Ref. 7)

$$CR = \frac{\text{Aperture area}}{\text{Receiver area}} = \frac{W - D_r}{\pi D_r}$$

Equation 3.3

The surface area of the solar receiver (A_r) tube is calculated from the Equation 3.4 (Ref. 7)

$$A_r = \pi D_r L_r$$

Equation 3.4

where D_r is receiver diameter and where L_r is receiver length.

In determining the position of point P on the Earth's surface concerning solar radiation, the parameters essential for designing a solar tracking system can be computed at any given moment, provided the latitude (l), the hour angle (w), and the Sun's declination angle (d) are known for that particular location. The declination angle (d) represents the Sun's angular position at solar noon concerning the equator, typically falling within the range of 23.45° ≤ δ ≤ 23.45°, as determined by employing Equation 3.5 (Reference: 7).

$$\delta = 23.45 \sin\left(360 \times \frac{284 + n}{365}\right)$$

Equation 3.5

The angle of each hour (*w*) is obtained from:

$$\square = 15(12 \square st)$$

The local standard time (*st)* compared with solar noon, an area test, is obtained from:

$$st = \text{Standard time} + E - 4(\text{Long} \square \text{Long})$$

Experimental Setup

The experimental setup involved the utilization of the described experimental system. This system consisted of a solar parabolic trough collector (SPTC) arranged with the long axis of the parabola aligned in the north-south direction, facilitating the collection of solar radiation in the east-west orientation. Comprising three SPTs, each sized at 1200 × 1520 mm² with a 300 mm focal length, these collectors focused sunlight at the focal point. The components of the collector and solar parabolic trough assembly encompassed: (i) solar receiver vacuum tube, (ii) solar parabolic trough collector, (iii) solar hot water tank, and (iv) Sun tracking system. An illustration of the components and the schematic diagram of the system is presented in Figure 3.2. The specific solar tracking system designed for the SPT is depicted in Figure 3.3, while the detailed characteristics of the SPT are outlined in Table 3.1.

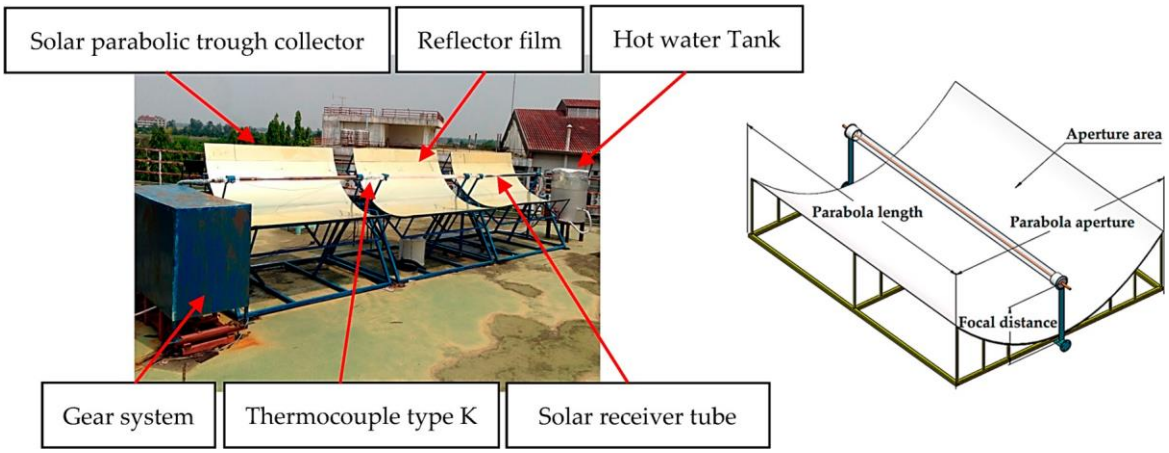

Figure 3.2: The solar parabolic trough collector and schematic diagram of the SPTC (Ref. 7)

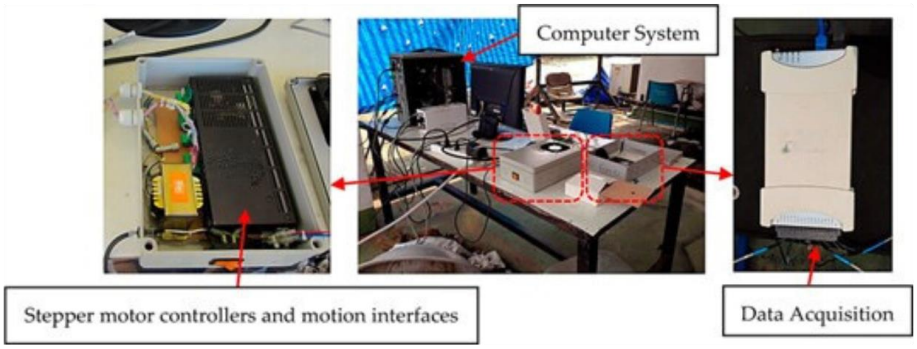

Figure 3.3: The solar tracking and data acquisition systems for the SPTC (Ref. 7)

No.	Parameter	Characteristics
1	Parabola length (*L*)	1520 mm
2	Parabola aperture (*W*)	1200 mm
3	Focal distance (*f*)	300 mm
4	Thickness (mean value)	3 mm
5	Aperture area (A_a)	2.09 m²
6	Collector length (*L*)	1.52 m
7	Concentration ratio (*CR*)	8.13

Table 3.1: Characteristics of each solar parabolic trough collector (SPTC) set (Ref. 7)

The depicted Figure 3.4 highlights the components and geometric specifications of the solar absorber vacuum tube assembly employed in the experiment. Two variations of absorber tubes were under assessment: (a) smooth copper tubes and (b) finned copper tubes. These absorber tubes were arranged coaxially within an evacuated glass tube to minimize thermal losses from the absorber tube. The essential design parameters of these tubes are detailed in Table 3.2.

No.	Parameter	Volume/Type
1	Receiver material	copper
2	Receiver surface treatment	Heat-resistant black coating
3	Inner copper tube diameter (D_{ci})	10 mm
4	Outer copper tube diameter (D_{co})	12.70 mm
5	Inner glass cover diameter (D_{gi})	33.50 mm
6	Outer glass cover diameter (D_{go})	47 mm
7	Glass envelope transmissivity	0.95
8	Receiver length (L_r)	1.52 m
9	Receiver surface area (A_r)	0.23 m^2

Table 3.2: Parameters of the solar receiver tubes (Ref. 7)

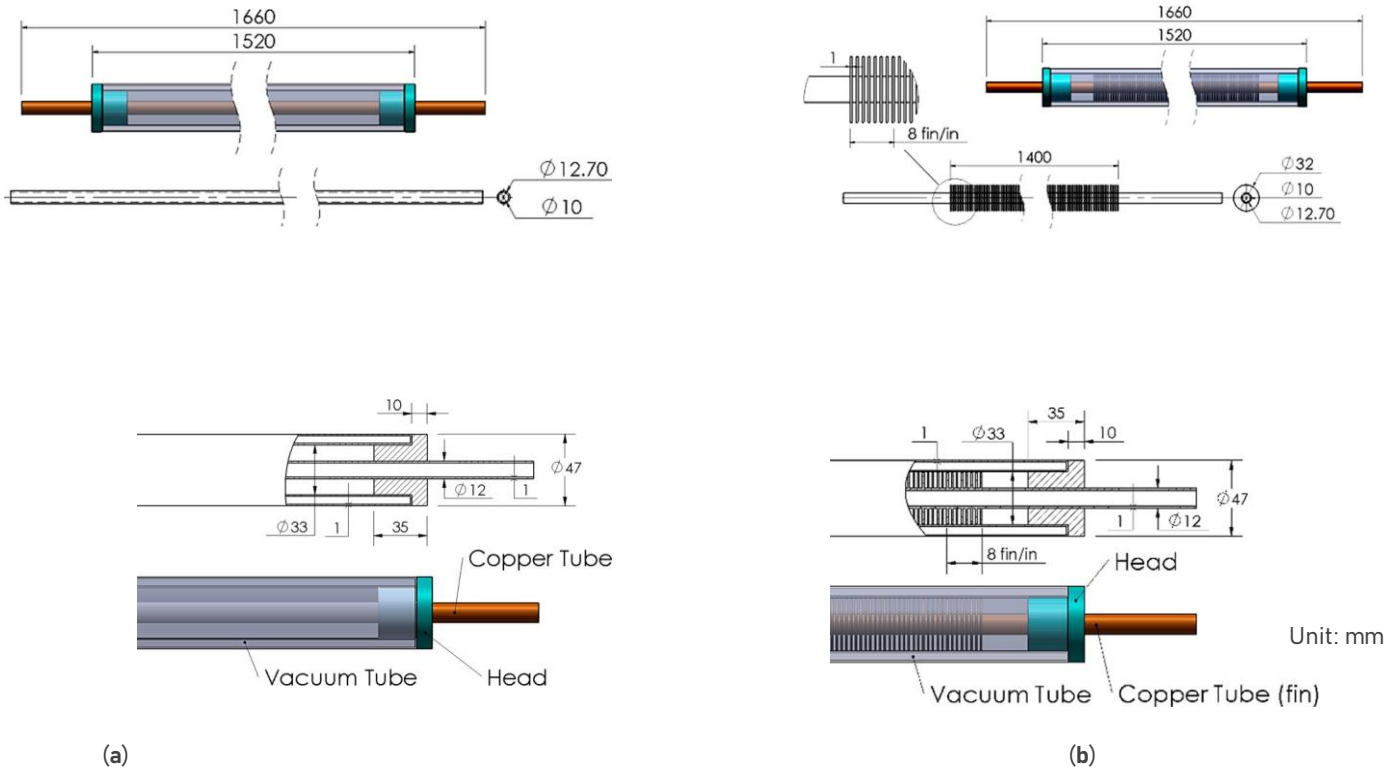

Figure 3.4: Geometrical parameters of the solar receiver tubes: (a) smooth copper tube and (b) finned copper tube (Ref. 7)

The experiment involved measuring the temperature of the circulating heat transfer fluid, in this case, water, at designated test points T1 to T4 located on the absorber tubes. Simultaneously, the local ambient air temperature (Ta) was also recorded. These measurement points, T1, T2, T3, and T4, were situated at a distance of 1.7 meters from each other, in accordance with Figure 3.4. The absorber tube's glass envelope exhibited an external diameter of 47 mm and an internal diameter of 33 mm. Within this glass envelope, the copper absorber tube was positioned coaxially, and the envelope was evacuated to assist in retaining heat, as visually depicted in Figure 3.5.

.

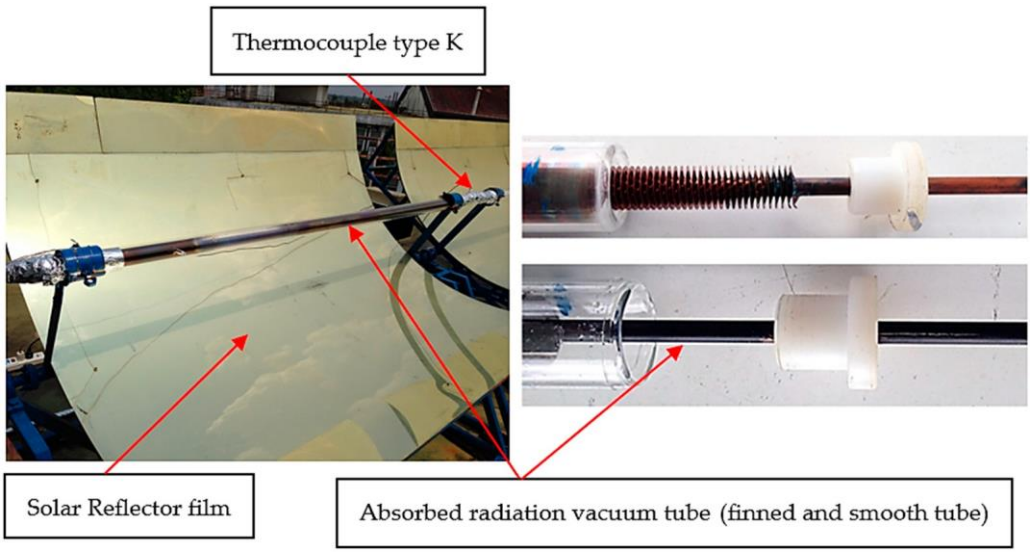

Figure 3.5: Absorber vacuum tube assemblies for smooth and finned tubes (Ref. 7)

Solar Radiation with Time

Figure 4 depicts the fluctuation in solar radiation over time throughout a 20-day experimental period. Data analysis focused solely on the 10 days characterized by minimal cloud cover. Notably, the total solar energy received by the collector remained nearly constant across all days. As anticipated, solar radiation exhibited time-dependent behavior, with a notable surge between 10:00 and 11:00. During the morning hours, solar radiation levels ranged between 474.45 to 1127.84 W/m2, peaking from 11:00 to 13:00, and gradually declining from 13:00 to 16:00.

The average solar radiation recorded over these 10 selected days during the experiment amounted to 834.61 W/m2. This solar radiation pattern aligns with typical conditions experienced for approximately 8 to 10 months per year in Thailand, indicating favorable performance of the PTC (Parabolic Trough Collector) for the majority of the year. However, in real-world applications, measured solar power values may vary due to additional atmospheric influences such as wind, pollution, and atmospheric dust. These factors can potentially lead to a reduction in the portion of solar radiation reaching the collector.

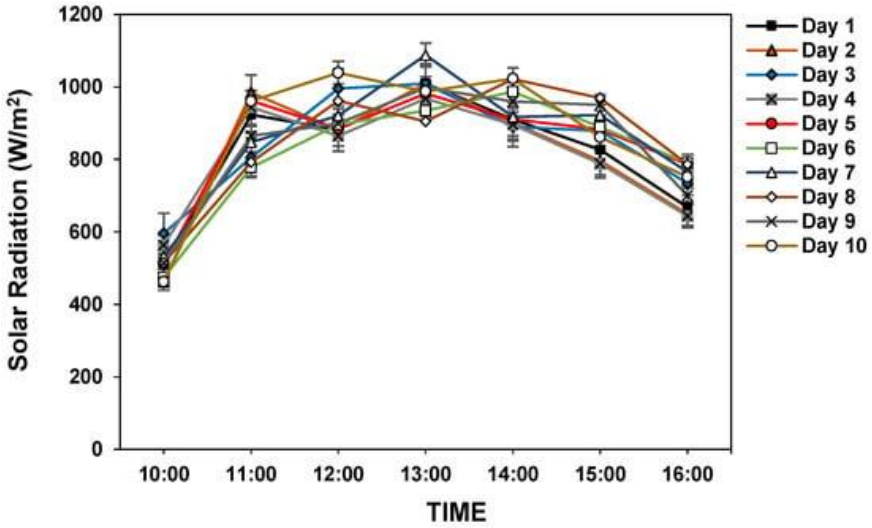

Figure 4: Variation in solar radiation with time (Ref. 7)

The Solar Tracking System

Throughout the experiments, the SPT system was oriented with the long axis of its parabolic trough aligned north-south, enabling the collection of solar radiation in the east-west direction. The solar tracking system managed the movement of the SPT unit, initially positioned towards the east.

For the program to commence, the user was required to input location details, time zone, and local time into the software. Following these configurations, the system was prepared for operation. The SPT tracked the Sun's daily path by rotating the SPT axis from east to west at a consistent speed of 0.00415 degrees per second, utilizing a stepping motor linked to a gearbox specifically designed for a total rotation of 15 degrees per hour. At the end of each day, the SPT returned to its initial starting position.

The experiment was conducted from March 11 to March 30, corresponding to Thailand's summer season, aligning with days 70 to 89 for that year. The declination angle (δ) of the Sun was calculated to be within the range of -4.41° to 3.22°. Equation 4.1 details the angle of incidence for the SPT along a north-south axis with a continuous east-to-west trajectory. This calculation resulted in an angle within the range of 0.997 ≤ cosθ ≤ 0.998.

$$cos\theta = cos\delta$$

where θ is the Sun's incident angle and δ is the Sun's declination angle.

Equation 4.1

The concentrating solar system implemented a horizontal single-axis solar tracking control system. Consequently, the incident angle of the Sun (θ) significantly influenced the effective daylight area (Aa) of the aperture area. To derive the effective intensity of sunlight reaching the collection area, considering both the solar intensity on the aperture area and the variable angle of incidence resulting from seasonal changes, Equation 4.2 (Reference: 7) is used for this purpose.

$$I_{eff} = I_b cos\theta$$

Equation 4.2

where I_{eff} is the effective intensity of sunlight falling on the collection area, I_b is the local direct solar light intensity, and θ is the Sun's incident angle.

Derived from the aforementioned equations, the effective intensity of solar radiation ranged between 0.997Ib and 0.998Ib, signifying a close approximation to direct solar radiation. Hence, one can reasonably utilize the simplification Ieff ≈ Ib in calculations throughout this experiment.

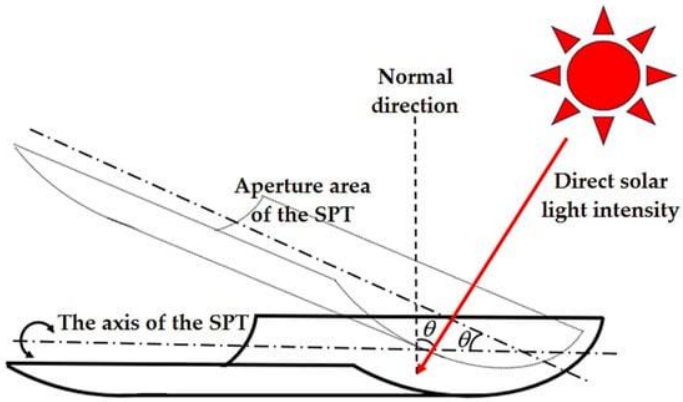

Figure 4.2: The effect of the angle of incidence of the Sun on the aperture area (Ref. 7)

Installation Overview

The establishment of the 200kW Stirling generator plant in Thailand involved a series of structured installation steps. This section aims to outline the procedural methodologies and key tasks undertaken during the installation process.

I. **Site Preparation and Planning**

Prior to installation, extensive site evaluation and planning were conducted. Site suitability, land assessment, and compliance with local regulations were essential considerations. Detailed engineering surveys were carried out to identify optimal positioning for solar collectors and associated infrastructure.

II. **Foundation and Infrastructure Setup**

The initial phase involved laying the groundwork, including the construction of necessary foundations for the Stirling generator, solar collectors, and ancillary equipment. This step encompassed structural assembly, civil works, and any necessary groundwork for efficient plant operation.

III. **Solar Collector Assembly**

The installation of solar collectors was a critical aspect of the setup. The collectors were strategically positioned and aligned to maximize solar exposure and capture. A systematic assembly process was employed to ensure precise alignment and integration of individual collector units.

IV. **Stirling Engine Installation**

The Stirling engine assembly and installation required meticulous adherence to technical specifications. This phase involved the positioning and secure mounting of the Stirling engine, including essential components such as the crankshaft, pistons, heat exchangers, and the alternator, among others.

V. **Electrical Integration and Connection**

The electrical components, including wiring, control systems, and power management units, were integrated. Connections were established between the Stirling engine and the power distribution network, ensuring seamless integration into the electrical grid.

VI. **Performance Testing and Commissioning**

After installation, rigorous performance tests were conducted to validate the operational efficiency and reliability of the Stirling generator plant. Comprehensive testing included functional checks, load testing, and calibration to ensure adherence to operational parameters.

The successful installation of a 200kW Stirling generator plant in Thailand involved a systematic approach encompassing site preparation, meticulous assembly, electrical integration, and comprehensive testing. The culmination of these steps led to the functional commissioning of the plant, paving the way for sustainable and efficient energy production.

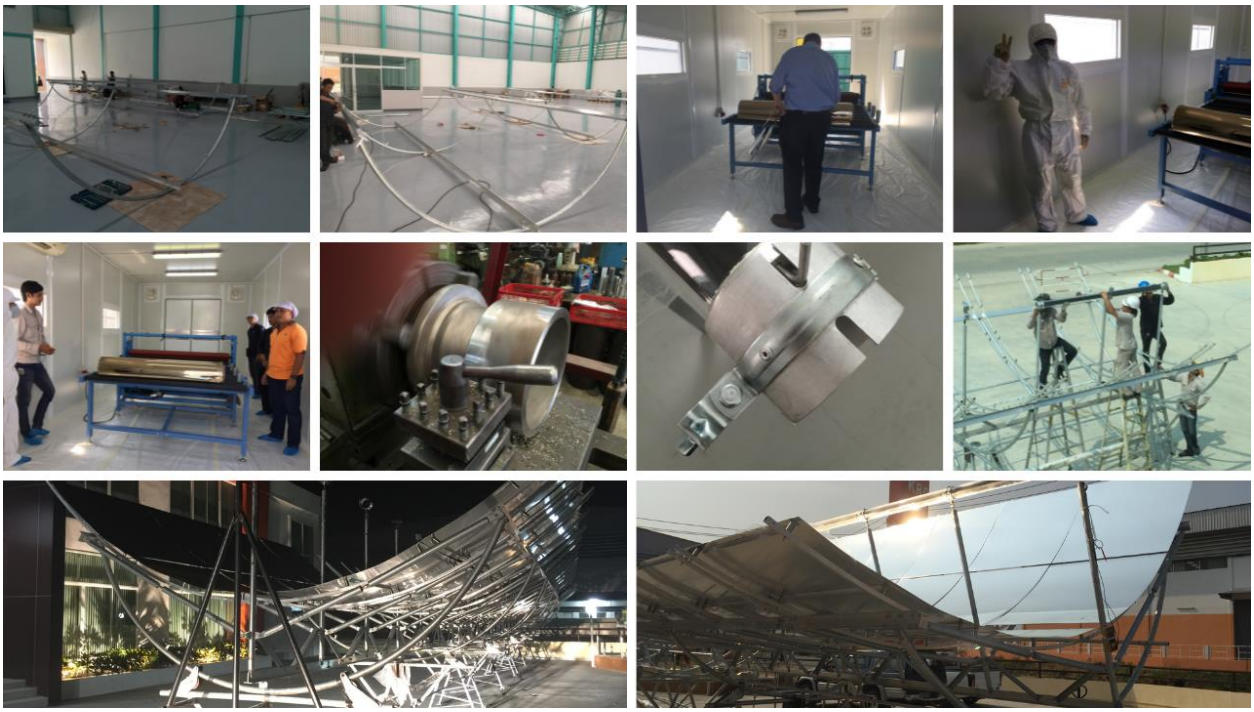

Image 2.1 Plant Construction & Installation

Results

The integration of the Stirling generator yielded significant benefits:

1. **Efficiency Gains**: The power generation facility saw a notable increase in efficiency, resulting in cost savings and reduced fuel consumption.
2. **Emissions Reduction**: Greenhouse gas emissions were reduced, aligning with environmental sustainability goals.
3. **Improved Reliability**: The Stirling generator proved to be a more reliable source of power, reducing downtime and improving the stability of the power supply.

The Solar Stirling represents a noteworthy advancement in solar collector technology, resulting in an innovative, modular collector design that combines a sturdy yet lightweight synthetic construction of a tested composite panel, an efficient thin-glass mirror, and minimized steel components. This project, which commenced in 2015, has yielded valuable insights that underscore its competitive edge in the field. Key lessons learned include

- **Optimized Collector Design:** The parabolic design of the collector was meticulously aligned with the characteristics of the vacuum receiver. Each collector measures 12 meters in length, equivalent to the length of three receivers. These collectors are grouped into modules, with each module accommodating twelve collectors. Furthermore, the collector is comprised of segments, each spanning 12 meters and accommodating three receivers. Consequently, the length of a collector module is set at 120 meters.
- **Higher Operating Temperatures:** The redesigned parabolic trough collector can facilitate higher operating temperatures, reaching up to 650 °C. This enhancement is a testament to improved design and superior optical properties.
- **Simplified Construction:** The improved construction techniques have led to increased rigidity and enhanced wind resistance, streamlining the overall manufacturing process.

- **Reduced Collector Weight:** By reducing the steel content in the collector's construction, a substantial reduction in the collector's weight has been achieved. This weight reduction not only enhances the collector's practicality but also its economic feasibility.
- **Cost Reductions**: The innovative design has significantly reduced the overall costs associated with the collector. In particular, cost reductions have been observed in both production and transportation. Notably, the modular nature of the collector allows for easy shipment in standard containers, obviating the need for on-site manufacturing. This modularity further affords the flexibility to accommodate projects of varying sizes.
- **Enhanced Optical Efficiency:** The newly developed parabolic trough collector attains an optical efficiency rating of up to 92%. This substantial increase in optical efficiency represents a significant leap forward in harnessing solar energy.

The Solar Stirling project has yielded a solar collector system that excels in various critical aspects, ranging from optimized design and elevated operating temperatures to simplified construction, reduced weight, and notable cost savings. Additionally, the collector's enhanced optical efficiency underscores its technical and economic viability, marking a substantial advancement in solar collector technology.

The System produces 6,800 kWh of Thermal Energy output and 4,800 kWh of electrical output per 24 hours, maintaining a constant hourly output of 200kW electrical energy. The plant has a footprint of 2000-3500m2. The cost of the electrical energy remains low, with thermal energy often regarded as a complimentary or negligible component if not commercially utilized.

Future Outlook

When relocating the same facility to different regions, such as the northern or southern hemisphere (Scandinavia, Canada, South Australia, South Africa, South America), seasonal variations in solar irradiation must be considered. Systems can be designed to compensate for these differences, ensuring a guaranteed minimum energy output during low-sun months. While this may entail additional costs, the value of having thermal energy available greatly offsets them. The relative Levelized Cost of Electricity (LCOE) typically does not exceed $0.15 USD for electricity only, with a guarantee of electricity supply around the clock for most of the year.

In regions characterized by extended periods of extremely low solar irradiation, such as very northern or southern latitudes, combining the Stirling Generator with wind turbines or biomass boilers proves economically advantageous. The Stirling Generator can absorb and store surplus energy from these sources, ensuring optimal production and demand alignment. Another synergistic integration in such areas involves circular hydrogen facilities, producing hydrogen during high-energy seasons, storing it for extended periods, and utilizing it during low-energy periods through fuel cells. Hydrogen production via electrolyzers and electricity conversion via fuel cells generate heat output that can be captured and cycled back into the system, creating a holistic and efficient energy ecosystem.

Conclusion

The case study highlights the successful integration of a Stirling generator into a power generation plant, achieving enhanced efficiency, reduced emissions, and improved reliability. The project underscores the potential of Stirling engines in addressing the growing need for more sustainable and efficient energy solutions.

References

1. Liaw Geok Pheng; Rosnani Affand; ,Mohd Ruddin Ab Ghani; Chin Kim Gan; Zanariah Jano; Tole Sutikno; A Review of Parabolic Dish-Stirling Engine System Based on Concentrating Solar Power, December 2014
2. Terence West; 17-06-2023
3. DLR; Prof. Dr.-Ing.; Robert Pitz-Paal (Director, Institute of Solar Research); Cologne, May2021
4. Nils Breidenbach et al. / Energy Procedia 99 (2016)
5. Songgang Qiu; Laura Solomon; Garrett Rinker; Development of an Integrated Thermal Energy Storage and Free-Piston Stirling Generator for a Concentrating Solar Power System, 8 September 2017
6. Jonathan F. Metscher; Edward J. Lewandowski; Development and Validation of Linear Alternator Models for the Advanced Stirling Convertor, NASA, Glenn Research Center, Cleveland, Ohio, 2015
7. Teerapath Limboonruang; Muyiwa Oyinlola; Dani Harmanto; Pracha Bunyawanichakul; Nittalin Phunapai; Optimizing Solar Parabolic Trough Receivers with External Fins: An Experimental Study on Enhancing Heat Transfer and Thermal Efficiency, 2023
8. Luke Saindon; Thermodynamic Theory of the Ideal Stirling Engine, 2019